ABSTRACT

Title of Dissertation: NANOPHOTONIC DEVICES BASED ON LOW-DIMENSIONAL QUANTUM EMITTERS

Zhili Yang, Doctor of Philosophy, 2018

Dissertation directed by: Professor Edo Waks,
Department of Electrical and Computer Engineer

Development of advanced nanophotonic devices is currently in rapid growth and revolutionizing the whole fields of integrated optics and photonics. Devices such as nanoscale LEDs & lasers, waveguide couplers and modulators are essential components in applications ranging from light sources to optical circuits and quantum information processing. The optical characteristics of these nanostructures could be engineered to realize strong confinement of optical modes within their low dimensions, which leads to strong light-matter interactions at desirable wavelength range when coupling to high-efficient, low-dimensional quantum emitters such as colloidal nanoplatelets, perovskite nanocrystals and transition metal dichalcogenide monolayers with unique optical properties. These light-matter coupled systems could realize various kinds of nanophotonic devices with high efficiency and nonlinearity in development of more complex optical circuits and quantum networks.

In this thesis, I present my work first on experimental demonstration of spontaneous emission intensity and rate enhancement of both colloidal cadmium selenide/cadmium sulfide core/shell nanoplatelet and cesium halide bromide perovskite nanocrystals in Purcell regime by using silicon nitride photonic crystal nanobeam cavities. The one-dimensional high-quality cavity confines the emission in a small mode volume with high radiative decay mode density, leading to a clear increase in their photoluminescence efficiencies. We next present realization of a continuous-wave nanolaser based on this coupled system operating at room temperature. The high coupling efficiency results in a record-low pump threshold at 1 μW. This result shows that colloidal nanocrystals are suitable for compact and efficient opto-electronic devices based on solution-processable materials.

Besides light generation, furthermore for transmission and processing, we have also realized chiral light-matter interactions in a glide-plane photonic crystal waveguide using spin-valley states in transition metal dichalcogenides tungsten diselenide monolayers. The combination between the unique spin-valley coupling effect of this monolayer material and the chirality of the waveguide leads to a control over the propagation direction based on the helicity of input signal. This system enables on-chip directional control of light and could provide new ways for controlling spin and valley degrees of freedom in a scalable photonic platform.

NANOPHOTONIC DEVICES BASED ON LOW-DIMENSIONAL QUANTUM EMITTERS

by

Zhili Yang

Dissertation submitted to the Faculty of the Graduate School of the
University of Maryland, College Park, in partial fulfillment
of the requirements for the degree of
Doctor of Philosophy
2018

Advisory Committee:
Professor Edo Waks, Chair
Professor Thomas E. Murphy
Professor Jeremy N. Munday
Professor Mario Dagenais
Professor Luis Orozco

Dedication

I dedicate this thesis to my beloved families.

Acknowledgements

It is a true honor for me to have worked with many talented persons with great personalities during this past five-year journey at University of Maryland, pursuing my Ph.D. degree. I would like to take this chance to express my gratitude to these people who has helped me along the way. First of all, I would like to thank my advisor Professor Edo Waks for his outstanding guidance and support throughout my entire program. I learned a lot from his passion in science, rigorousness in research and especially the way of thinking and acting when facing problems. I am also thankful for his guidance in how to formalize and express my thoughts and ideas in research, which is crucial for my future career.

I would like to thank Professor Luis Orozco, Professor Thomas Murphy, Professor Jeremy Munday, and Professor Mario Dagenais for being on my dissertation defense committee. I would also like to thank Professor Matthew Pelton, who is not only an important collaborator for different research of ours, but also a great mentor to me. I would also like to express my gratitude to my collaborators including Professor Dmitri V. Talapin, Professor Maksym V. Kovalenko, Dr. Maryna I. Bodnarchuk and Dr. Igor Fedin. None of my research goals could be achieved without their genuine support and help.

I would like to acknowledge my past and present colleages in our group for their support: Dr. Shilpi Gupta, Dr. Kangmook Lim, Dr. Shuo Sun, Dr. Tao Cai, Dr. Je-hyung Kim, Dr. Hirokazu Miyake, Dr. Jose Algarin, Shahriar Aghaeimeibodi,

Sabyasachi Barik, Zhouchen Luo, Aziz Karasahin, Subhojit Dutta, Mustafa Atabey Büyükkaya, Dr. Chang-Min Lee and Dr. Youngmin Martin Kim.

I acknowledge support from technicians in the UMD nanofabrication center: Tom Loughran, Jon Hummel, John Abrahams, and Sz-Chian Liou. I thank them all for maintaining the equipments in a good shape and always being there to help when necessary. I would also like to thank all the staff members in IREAP and ECE departments, past and present, Jay Pyle, Nolan Ballew, Bryan Quinn, Ed Condon, Nancy Boone, Dorothea Brosius, Melanie Prange, Vivian Lu, Bill Churma, Emily Irwin, and Maria Hoo.

Finally, I would like to thank my families for their unconditional love and support. It means a lot to me especially when being aboard for these years.

Table of Contents

List of Figures

List of Abbreviations

TMD	transition metal dichalcogenide
CW	continuous-wave
SiN	silicon nitride
$CsPbBr_3$	cesium halide bromide
TEM	transmission electron microscope
CdSe	cadmium selenide
CdS	cadmium sulfide
CVD	chemical vapor deposition
WSe_2	tungsten diselenide
SEM	scanning electron microscope
CMOS	complementary metal oxide semiconductor

Chapter 1: Introduction

1.1 Overview

Development of advanced nanophotonic devices is currently in rapid growth and revolutionizing the whole fields of integrated optics and photonics[1,2]. Devices such as nanoscale LEDs & lasers, waveguide couplers, modulators and detectors are essential components in applications ranging from light sources to optical circuits and quantum information processing. The optical characteristics of these photonic nanostructures could be engineered to realize strong confinement of optical modes within their low dimensions, which leads to strong light-matter interactions when coupling to low-dimensional quantum emitters such as colloidal nanoplatelets[3], perovskite nanocrystals[4] and transition metal dichalcogenide (TMD) monolayers[5] with wide wavelength tunability and high efficiency. These light-matter coupled systems could realize various kinds of linear/nonlinear, active/passive nanophotonic devices at single photon operation level, in order to develop more complex optical circuits and quantum networks.

The first essential component in optical circuits and networks is nanoscale laser, which could act as a coherent power source for all other elements and also as the carrier of signals. In order to realize such nanoscale lasers with low energy consumption, solution-processed emitters offer a compelling gain material. These materials can be synthesized using inexpensive colloidal chemistry techniques, alleviating the need for complex epitaxial deposition methods. They can also be placed on a broad range of substrates using convenient solution-deposition techniques. For example, fluorescent

molecules embedded in polymer can act as a gain material for lasers[6]. However, these emitters typically photo-bleach on short timescales of seconds to minutes[7], and also suffer from rapid gain quenching due to intersystem crossing into dark triplet states, making continuous-wave (CW) operation challenging[6]. Colloidally synthesized quantum wires have also shown lasing with the possibility of electrical injection[8]. However, the optical mode in nanowire lasers extends for several microns along the wire axis, resulting in high threshold pump powers[9].

Semiconductor nanocrystals synthesized by colloidal chemistry have emerged as another promising solution-processable gain medium[10]. They exhibit significantly better photostability than fluorescent molecules[11] and do not suffer from gain quenching due to intersystem crossing. Perhaps the most well-studied nanocrystal emitters are quantum dots, which have historically suffered from rapid Auger recombination that made lasing difficult to achieve[12]. However, recent advances in quantum-dot synthesis have largely mitigated this problem and enabled amplified spontaneous emission and lasing in large-mode-volume cavities such as Fabry–Pérot, distributed Bragg reflector, and microsphere cavity resonators over the entire visible spectral range[13-18] and extending out to infrared frequencies[19]. In addition to quantum dots, new colloidal materials such as nanorods[20,21], nanoplatelets[22-25] and perovskite nanocrystals[26,27] have emerged as good gain materials for room-temperature amplified spontaneous emission and lasing. However, all of the past work required large pump powers in the milliWatt to kiloWatt range to achieve lasing threshold due to their large cavity mode volume and high loss.

One way to significantly reduce these large threshold powers is to employ small mode-volume cavities that reduce the size of the active material and enhance the spontaneous emission coupling efficiency[28]. Nano-lasers based on various materials have been previously demonstrated using both dielectric cavities[29] and metallic nanostructures[30]. However, the development of nano-lasers using solution-processable semiconductor nanocrystals has proved difficult. A number of works incorporated colloidal quantum dots into nanocavities[31-33], but were unable to reach lasing due to rapid Auger recombination which is a nonradiative process due to the high confinement of excitons and resulted in gain quenching[34]. The poor uniformity of quantum dot films deposited on nanophotonic structures also posed a major obstacle, and these films degraded rapidly under optical excitation[35]. Achieving a low-threshold nano-laser using such materials has remained an outstanding challenge.

In this thesis, we first demonstrate an experimental realization of a nano-laser using colloidally synthesized semiconductor nanocrystals. We utilize colloidal nanoplatelets, a new class of material, coupled to silicon nitride (SiN) nanobeam cavities to achieve CW room-temperature lasing. Colloidal nanoplatelets exhibit high gain and photostability, and also deposit as thin uniform films on top of the nanocavity, enabling us to overcome many of the challenges faced by previous efforts using quantum dots. We demonstrate lasing with a threshold input power of 0.97 μW, the lowest reported threshold for any laser using colloidal emitters. We also estimate an absorbed power of 210 nW, which is equivalent to the lowest reported value for a room-temperature laser[36]. Our results are an important step towards efficient on-chip light

emitters and photonic integrated devices based on colloidally synthesized solution-processable materials.

Similarly, we utilize a coupled system to demonstrate spontaneous emission intensity and Purcell rate enhancement of colloidal cesium halide bromide ($CsPbBr_3$) perovskite nanocrystals[37], which is another promising candidate for light-emitting materials besides used in solar cells to achieve high conversion efficiencies[38], if we could resolve the emitter degradation issue we encountered.

Besides light generation, furthermore for transmission and processing, we have also realized chiral light-matter interactions in a glide-plane photonic crystal waveguide[39] using spin-valley states in transition metal dichalcogenides tungsten diselenide monolayers[40]. The combination between the unique spin-valley coupling effect of this monolayer material and the chirality of the waveguide leads to a control over the propagation direction based on the helicity of input signal. This system enables on-chip directional control of light and could provide new ways for controlling spin and valley degrees of freedom in a scalable photonic platform.

1.2 Low dimensional quantum emitters

1.2.1 Colloidal nanoplatelets

Colloidal nanoplatelets have a few atomic layers thickness, which are thought as quantum well structures[3]. Carriers within the material are only confined quantum-mechanically in one dimension. Therefore, the exciton density is much less in the other two directions, leading to a smaller Auger recombination rate, which diminishs the

radiative emission efficiency of other materials such as quantum dots. In addition, they have almost no inhomogeneous broadening and photoluminescence from individual nanoplatelet resembles each other. These features are all in favor of material gain. Figure 1.1 and figure 1.2 show a transmission-electron-microscope (TEM) image and a schematic demonstrating the structure of the colloidally-synthesized cadmium selenide (CdSe) /cadmium sulfide (CdS) core/shell nanoplatelets from our collaborators at University at Chicago.

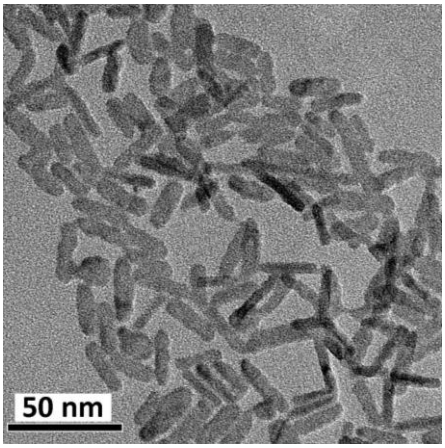

Figure 1.1 TEM image of nanoplatelets on glass

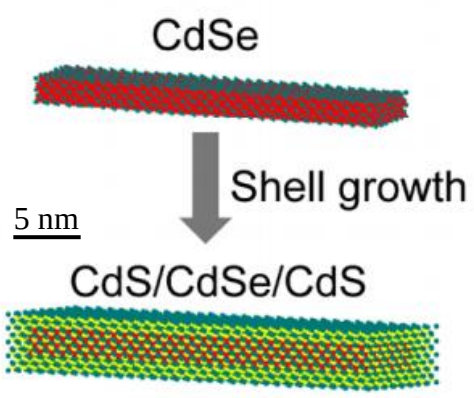

Figure 1.2 Schematic of CdSe/CdS core/shell nanoplatelet structure

1.2.2 Perovskite nanocrystals

Solution-processable lead trihalide perovskite semiconductors are also an alternative in optoelectronic applications to epitaxial materials that are complicated to synthesize[4,38,41,42]. They exhibit a small Stokes shift[43], high charge carrier mobility[44], and large absorption coefficient[45]. These features could lead to implementation of high-performance photovoltaic devices, light-emitting diodes, and light sources for efficient lasers. Previous studies focusing on photovoltaics have adopted perovskite thin films as an absorbing layer in solar cells with record-high certified conversion efficiencies of 22.1%[46]. Moreover, the material could serve as a new category of efficient emitters and gain materials in various light sources[47]. Figure 1.3 and figure 1.4 show a TEM image and a schematic demonstrating the structure of the perovskite nanocrystals from our collaborators in ETH.

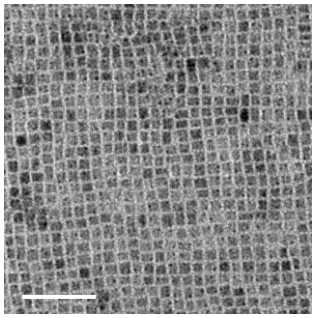

Figure 1.3 TEM image of $CsPbBr_3$ nanocrystals on glass (bar is 500 nm)

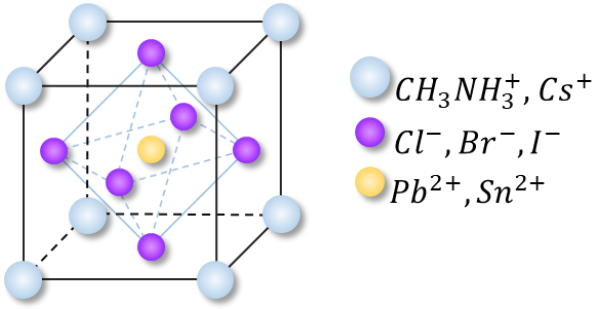

Figure 1.4 Schematic of perovskite nanocrystals

1.2.3 TMD monolayers

Recent discoveries and advances in group-VI transition metal dichalcogenide (TMD) monolayer materials have brought new possibilities and research interests to fields of photonics and optoelectronics[48,49]. When the materials with chemical composition MX_2 (M = Mo, W; X = Se, S), exfoliated into atomically thin monolayers, their indirect energy bandgaps in bulk formation become direct band[48]. Thus, unlike graphene with zero bandgap intrinsically[50], these optically active TMD monolayer materials are good candidates for integrated optics due to their 2D nature and bandgaps covering visible to near-infrared spectrum range[5,51]. The materials possess large exciton binding energy and high absorption because of the spatial confinement and reduced dielectric screening between charge carriers[52,53], which enables strong light-

matter interaction and even exciton devices at room temperature[54,55]. Their easily-controllable optical properties by doping, strain, and external fields could lead to realization of various devices such as LEDs and optical transistors[5,51]. The recent discovery of single photon emission in these materials from intrinsic [56-58] or strain-induced [59,60] defects further enables their applications in deterministic photon generation and quantum information and networks[2]. Figure 1.5 and figure 1.6 show optical images of chemical vapor deposition (CVD) grown tungsten diselenide (WSe_2) monolayer and schematic of TMD monolayers.

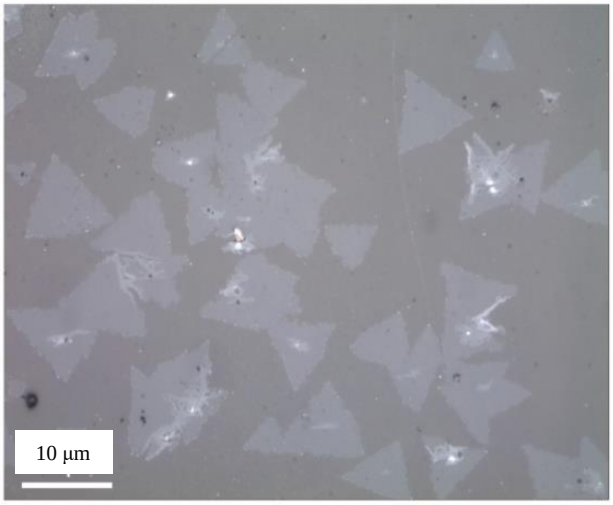

Figure 1.5 Optical image of WSe_2 monolayer on sapphire

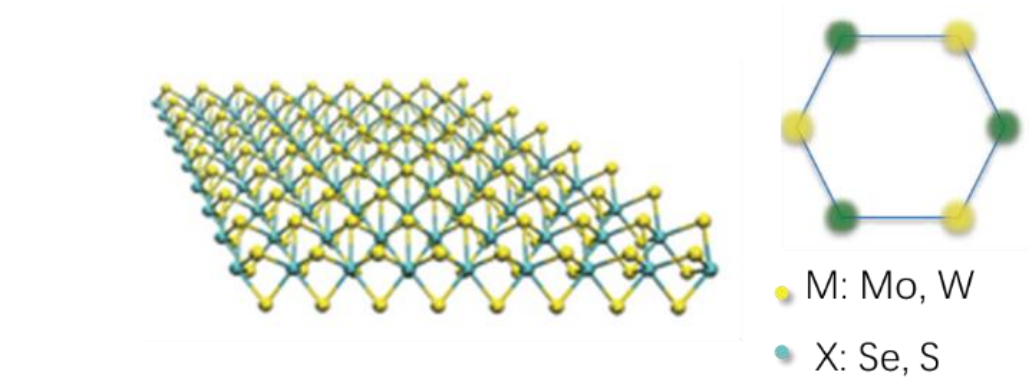

Figure 1.6 Schematic of TMD monolayer structure

1.3 Photonic crystals

Photonic crystals are periodic nanostructures fabricated on high refractive index dielectric materials, which lead to periodicity of refractive index in the length scale of optical wavelengths. In a photonic crystal, this periodic pattern generates constructive or destructive interference, which leads to optical Bragg scattering of photons. This is an analogous to an electron propagating in a real crystal with periodic lattices. In addition, one can engineer photonic crystals to open a photonic band gap, as a counterpart to electronic bandgaps in semiconductors, which prevents light propagation for a certain directions and wavelengths.

When introducing a localized disorder such as point defects in these 2D structures, a photonic state is formed within the bandgap, which can confine light locally and also modify the emission rate of luminescent materials by controlling the local density of states[61]. The properties of a photonic crystal cavity, such as the resonant frequency, quality factor, mode profile, and mode volume, can be easily controlled by modifying

the geometric properties of the photonic crystals[62]. In addition, a line defect can be function as a waveguide to transmit light in designed ways.

1.3.1 Photonic crystal cavity design

We adopt a nanobeam photonic-crystal cavity design. The cavity consists of a 200-nm-thick and 300-nm-wide silicon nitride beam with a one-dimensional periodic array of air holes (a = 250 nm and r = 70 nm for coupling to nanoplatelets). The cavity is formed by linearly reducing the lattice constant from 250 nm to 205 nm and the hole radius from 70 nm to 55 nm over a span of 4 holes from both sides of the center of the beam. This design results in a cavity with a resonance wavelength of 646 nm, and a calculated quality factor $Q = 1.1 \times 10^6$, obtained using numerical finite-difference time-domain simulations that assume perfect fabrication and less-free materials. Figure 1.7 shows the calculated electric field intensity profile of the fundamental mode overlap with the cavity structure. We also optimize another nanobeam cavity design for perovskite nanocrystals with a cavity resonance at 510 nm[63], with a $Q = 3.5 \times 10^4$.

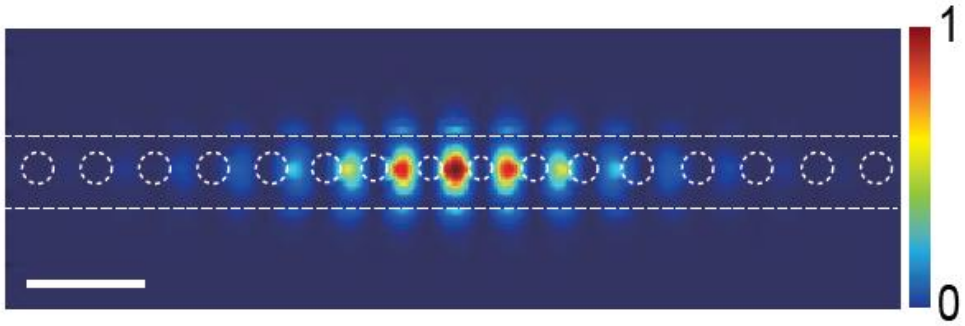

Figure 1.7 Calculated electric field intensity profile of the fundamental mode overlap with the cavity structure (bar is 500 nm)

Purcell factor of the cavity coupled system provides a lower bound on the fraction of spontaneous emission coupled into the cavity mode, which we denote as β. We define the Purcell factor as $F = \frac{\tau_{\text{sub}}}{\tau_{\text{c}}} = \frac{\gamma_{\text{c}}}{\gamma_{\text{sub}}}$, where τ_{sub} is the lifetime of nanoplatelets on the un-patterned substrate, τ_{c} is the lifetime of nanoplatelets coupled to the cavity, $\gamma_{\text{c}} = \frac{1}{\tau_{\text{c}}}$ is the decay rate of a nanoplatelet in the cavity, and $\gamma_{\text{sub}} = \frac{1}{\tau_{\text{sub}}}$ is the decay rate on the un-patterned substrate. The spontaneous emission coupling efficiency is given by $\beta = 1 - \gamma_{\text{leak}} / \gamma_{\text{c}}$, where $\gamma_{\text{c}} = \gamma_{\text{cav}} + \gamma_{\text{leak}}$; here, γ_{cav} is the nanoplatelet decay rate into the cavity mode and γ_{leak} is the decay rate of the nanoplatelets into all other radiative and non-radiative channels. An emitter inside of a cavity will typically experience Purcell enhancement when coupled to the cavity,[2] and Purcell suppression when decoupled (either due to detuning or poor spectral matching with the cavity),[3] which means that $\gamma_{\text{leak}} < \gamma_{\text{sub}}$. In this case $F < \frac{\gamma_{\text{c}}}{\gamma_{\text{leak}}}$ and thus $\beta > 1 - 1/F$. Using the relation $\beta > 1 - 1/F$, we obtain a lower bound of $\beta > 0.68$. This high coupling efficiency suggests that the devices should be able to support low-threshold lasing.

1.3.2 Device fabrication

We fabricated the devices on 200-nm-thick stoichiometric SiN deposited on silicon using low pressure chemical vapor deposition. We patterned the nanobeam photonic crystal cavities using electron-beam lithography and fluorine-based inductively coupled plasma dry etching. The underlying silicon was etched by aqueous

KOH to create a suspended beam. The scanning electron microscope (SEM) image of one final device is shown in figure 1.8.

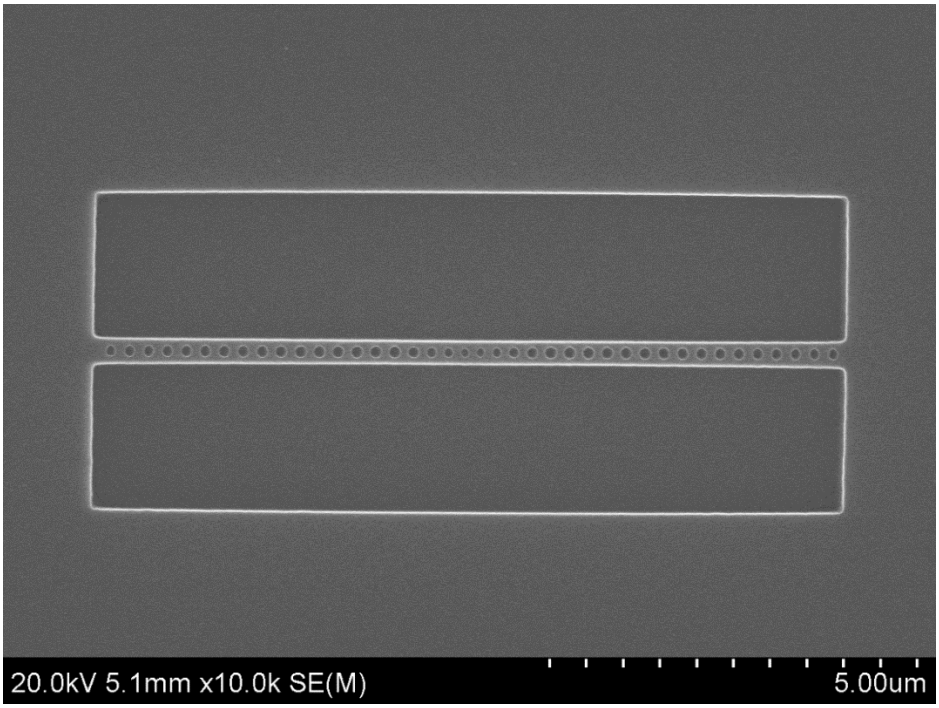

Figure 1.8 SEM image of SiN nanobeam cavity on silicon wafer

1.4 Outline of the thesis

This thesis presents studies in different nanophotonic devices based on low dimensional quantum emitters couple to photonic structures. Chapter 1 describes the motivations and goal of the studies. Chapter 2 focuses on the work in which we demonstrate a room temperature CW nano-laser using colloidal quantum wells coupled to a photonic crystal cavity. Chapter 3 presents cavity-induced spontaneous emission enhancement of colloidal perovskite nanocrystals. Chapter 4 introduces our work in realization of chiral light-matter interaction and directional light control using spin-

valley states in TMDs by coupling to a glide-plane photonic waveguide. Chapter 5 summaries the results shown in the thesis and discusses future directions.

Chapter 2 and 3 utilize systems with nanobeam cavities coupled to colloidal quantum emitters, which modify and enhance their emission spectrally and temporally in intensity and efficiency. The results lead to a highly efficient light source and nano lasers that are crucial in integrated optical systems. Chapter 4 is based on the unique spin-valley coupling property of TMD monolayers to introduce a new valley degree of freedom in light control and transmission. It brings potential research topics and applications such as transmission of valley spins in this new group of semiconductors and also new ways of on-chip directional control of light.

Chapter 2: A room temperature CW nano-laser using colloidal quantum wells

2.1 Fabrication of nano-laser

2.1.1 Colloidal gain material

The gain material for our nano-laser is a thin film of colloidally synthesized CdS/CdSe/CdS nanoplatelets. These semiconductor nanoscale heterostructures confine carriers quantum-mechanically in one dimension, and are thus the colloidal analogue of epitaxially grown quantum wells[3]. Colloidal nanoplatelets are promising materials for laser applications because they exhibit lower Auger recombination rates compared to those in conventional colloidal quantum dots at equivalent exciton densities,[64] and the core/shell structure significantly reduces emission intermittency (blinking) at a single nanoparticle level[65]. Thus, they can provide higher gain at equivalent excitation powers. Figure 2.1 shows the absorption and emission spectrum of the nanoplatelets used in our experiment, along with a TEM image. We provide a detailed description of the synthesis and characterization of the nanoplatelets in Appendix A.

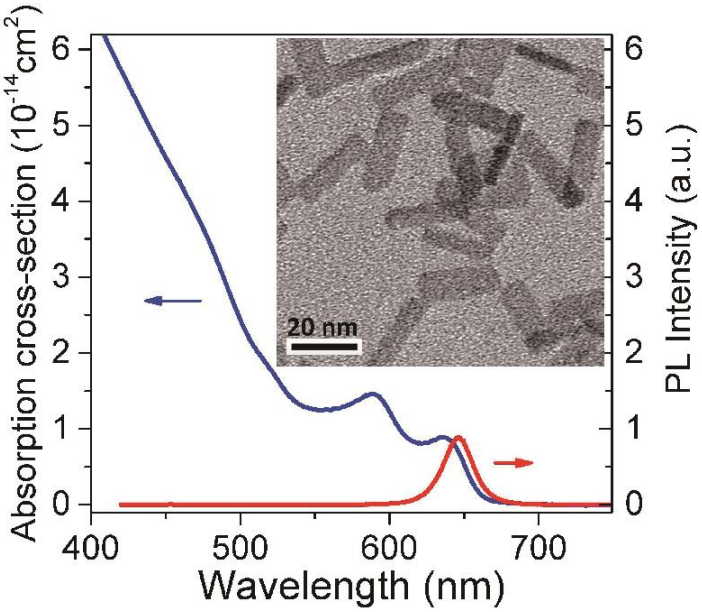

Figure 2.1 Absorption cross-section and photoluminescence spectra of CdSe core / CdS shell nanoplatelets in solution. The inset shows a TEM image of nanoplatelets.

2.1.2 Deposition on cavity

In order to create a nano-laser, we couple the nanoplatelets to a SiN photonic crystal nanobeam cavity[63]. SiN is an ideal substrate because it is highly transparent at the nanoplatelet emission wavelength and has a high index of refraction. It has the additional benefit that it can be fabricated with the same tools used for Si electronic devices[66], opening opportunities for complementary metal oxide semiconductor (CMOS) integration.

To fabricate the coupled device, we drop-cast a 10 nM nanoplatelet solution in a 9:1 mixture of hexane and octane onto the sample. From scanning electron microscope images of the device after deposition, we ascertain that the nanoplatelets are uniformly deposited on the surface of the devices, which is confirmed by consistent

photoluminescence emission intensity when exciting different regions on the sample. Figure 2.2 shows the coupled device with deposited nanoplatelet solution, the semitransparent area of holes indicates that the nanoplatelet film is uniformly covering the whole nanobeam cavity.

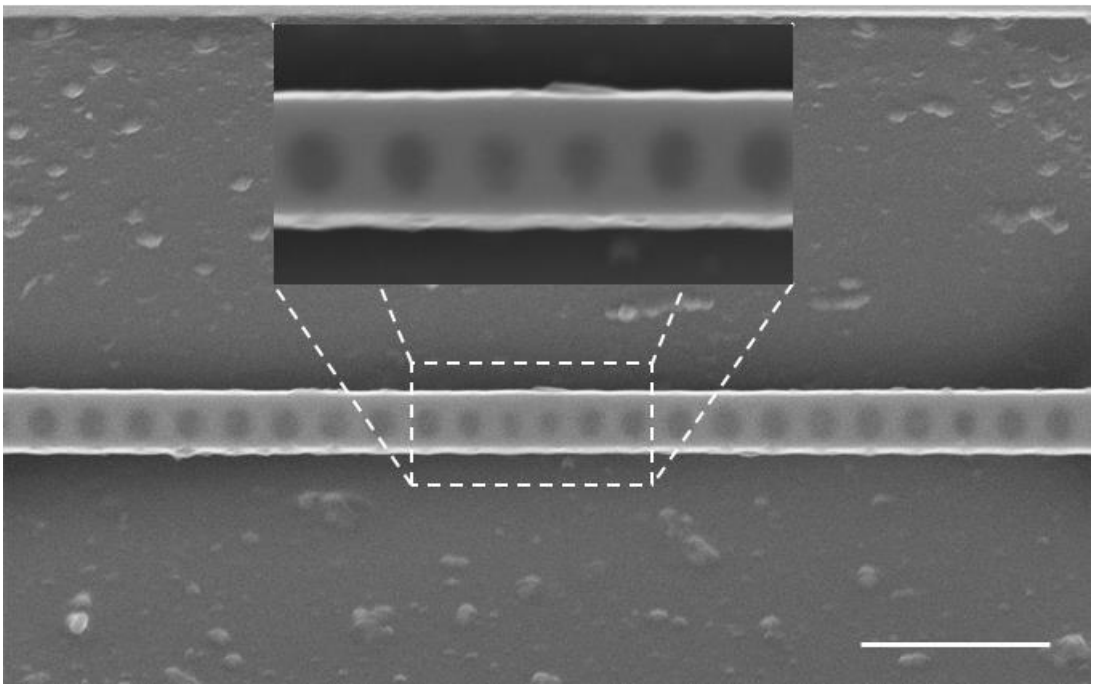

Figure 2.2 SEM image of nanobeam photonic crystal cavity after deposition of nanoplatelet solution (bar is 1 μm)

2.1.3 Measurement setup

The sample was loaded into a sealed chamber filled with purified nitrogen gas to avoid oxidation and photo-bleaching of nanoplatelets. Sample excitation and collection were performed by a confocal microscopy system using an objective lens with a numerical aperture of 0.6. The cavity emission signal was filtered out spectrally by a 600 nm long-pass filter and spatially using a pinhole aperture. We performed

polarization analysis using a half-wave plate and a polarizing beam-splitter. We used a continuous-wave 532.8-nm laser diode as an excitation source. We use the Gaussian beam formula given by $w = \frac{\lambda f}{\pi w_0}$ to estimate the pump spot size. In our experiment, the pump fills only 75 % of the input aperture, thus $\frac{w_0}{f} = 0.75 \times \mathrm{NA}$. By substituting these values into the above formula, we calculate a laser spot size of 0.38 μm in radius. The signal collected by the objective lens is focused into a grating spectrometer with a nitrogen-cooled CCD camera at one exit port to acquire the spectrum. To measure lifetime, we pump the sample using laser pulses with 70-ps duration at a wavelength of 405 nm. The laser pulse repetition rate is 20 MHz, and we set the average power to 1 μW. The collected signal is spectrally filtered by the spectrometer, and we detect the filtered signal using avalanche photodiode single-photon counters. A time interval analyzer correlates the detected photon events with the pump laser pulses to attain a lifetime trace. Figure 2.3 illustrates the experimental setup to characterize the fabricated devices.

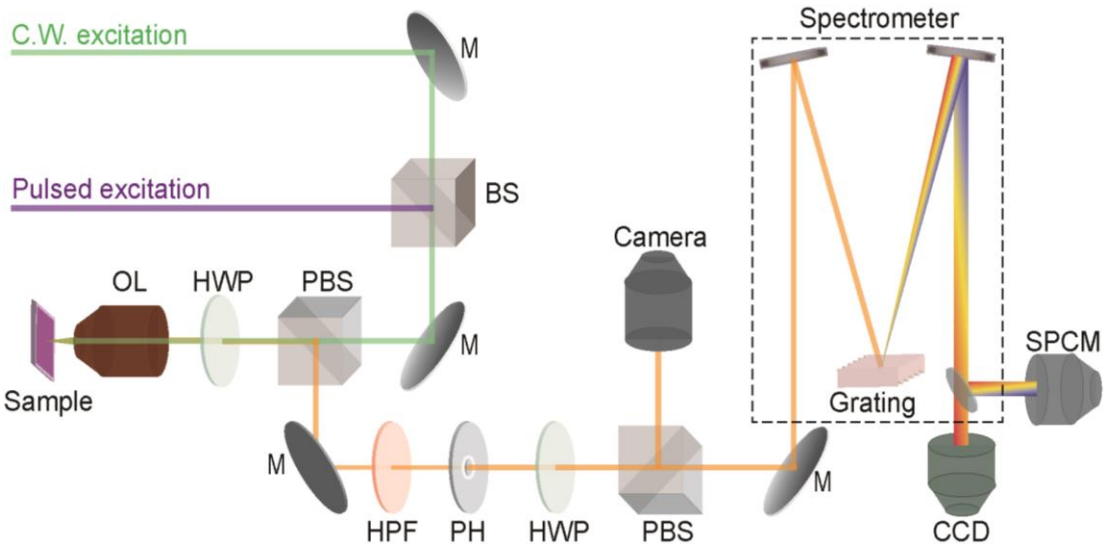

Figure 2.3 Experimental setup. M: mirror, BS: beam splitter, PBS: polarizing beam splitter, HWP: half wave plate, OL: objective lens, HPF: high-pass filter (cut off at 600 nm), PH: pin hole as spatial filter, SPCM: single photon counting module.

2.2 Photoluminescence measurement

2.2.1 Spectral enhancement

Figure 2.4 shows emission spectra obtained by exciting the nanoplatelets at the cavity region, as well as a reference spectrum from a region on the un-patterned sample surface (multiplied by a factor of 5 for better visualization). In both cases, we use an excitation power of 10 μW. The spectrum of the un-patterned region exhibits a full-width at half-maximum linewidth of 21 nm, which agrees with previously reported values for ensembles of nanoplatelets[3]. In contrast, the cavity emission shows a sharp resonance at the cavity center frequency that is more than 8 times brighter than the peak emission from the un-patterned surface. We attribute this increase in brightness to both

redirection of the nanoplatelet emission by the cavity as well as the Purcell effect (spontaneous emission enhancement into the cavity mode). We observe brighter intensity at the cavity resonance despite the fact that we excite many more nanoplatelets when looking at the bare surface as compared to the cavity, because the surface area of the nanocavity is much smaller than the surface area excited by the laser on the un-patterned surface. We calculate the surface area of the cavity, defined as the mode volume divided by the membrane thickness, to be 0.086 μm^2. In contrast, the illuminated surface area on the un-patterned surface is 0.45 μm^2.

The striking modification of the nanoplatelet emission spectrum is an indication of enhanced spontaneous emission from the nanoplatelets into the cavity mode. In addition, unlike the bulk emission, the emission from the cavity is highly polarized. The inset to figure 2.4 shows the spectra taken at polarization directions that are parallel and orthogonal with respect to the nanobeam. We obtain an emission polarization that is orthogonal to the nanobeam, in agreement with predictions from finite-difference time-domain simulations.

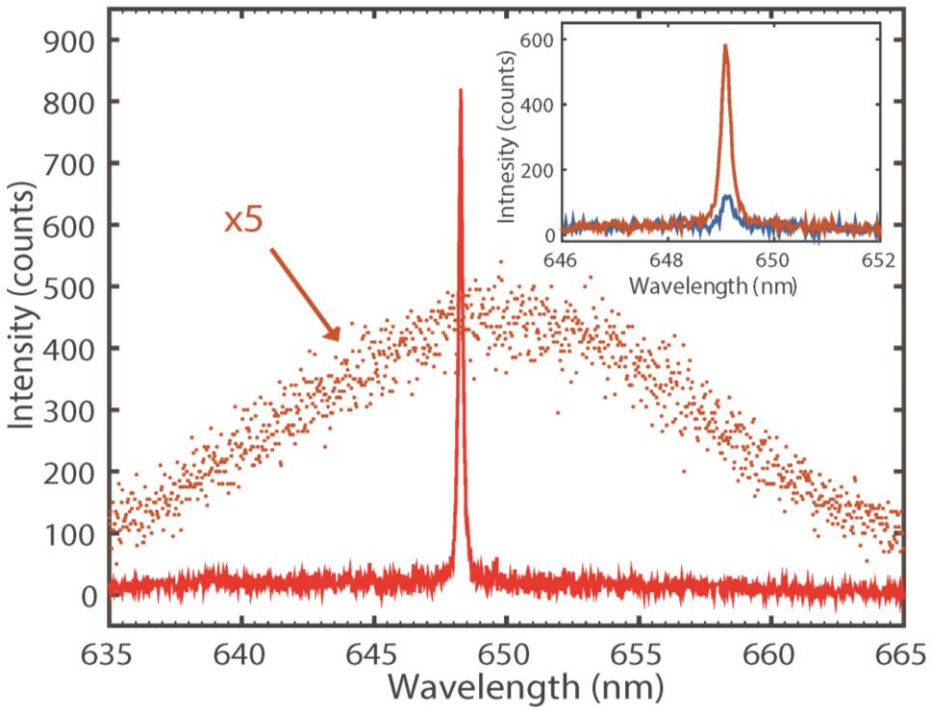

Figure 2.4 Emission spectra from nanoplatelets on the cavity (red) and in an un-patterned region (orange, multiplied by a factor of 5 for clarity), both measured under an excitation power of 10 μW. The inset shows emission spectra taken at polarization directions parallel (blue) and orthogonal (orange) to the nanobeam.

2.2.2 Purcell enhancement of radiative decay

In order to conclusively demonstrate that the nanocavity enhances the spontaneous emission of the nanoplatelets, we perform time-resolved measurements of the cavity emission. Figure 2.5 shows results for emission from the cavity and from the un-patterned surface. In both cases, the decay is bi-exponential, consistent with previous reports[67]. The fast decay component corresponds to direct radiative recombination of excitons in the nanoplatelet, and recent work has shown that the slow decay channel is likely due to other radiative decay channels involving localized states[68]. The constant background at long timescales (greater than 25 ns) is due to dark

counts and collection of residual background photons. Figure 2.6 shows a histogram of the decay times of the dominant fast decay rate, observed from 10 different devices. For each device, we measure both the cavity decay rate and the decay rate of the nearby un-patterned surface as a reference. The average lifetime of the un-patterned surface is 2.32 ± 0.22 ns, in good agreement with previous measurements. The cavity-coupled nanoplatelets exhibit a reduced lifetime of 0.74 ± 0.14 ns. We define the Purcell factor *F* as the ratio of these lifetimes. Figure 2.7 shows a histogram of the *F* obtained from all the devices. The average value of the Purcell factor is $\bar{F} = 3.1 \pm 0.3$. A similar analysis for the slow decay rate yields a Purcell factor of $\bar{F} = 2.7 \pm 0.3$, which supports the assertion that both channels correspond to radiative decay processes[68].

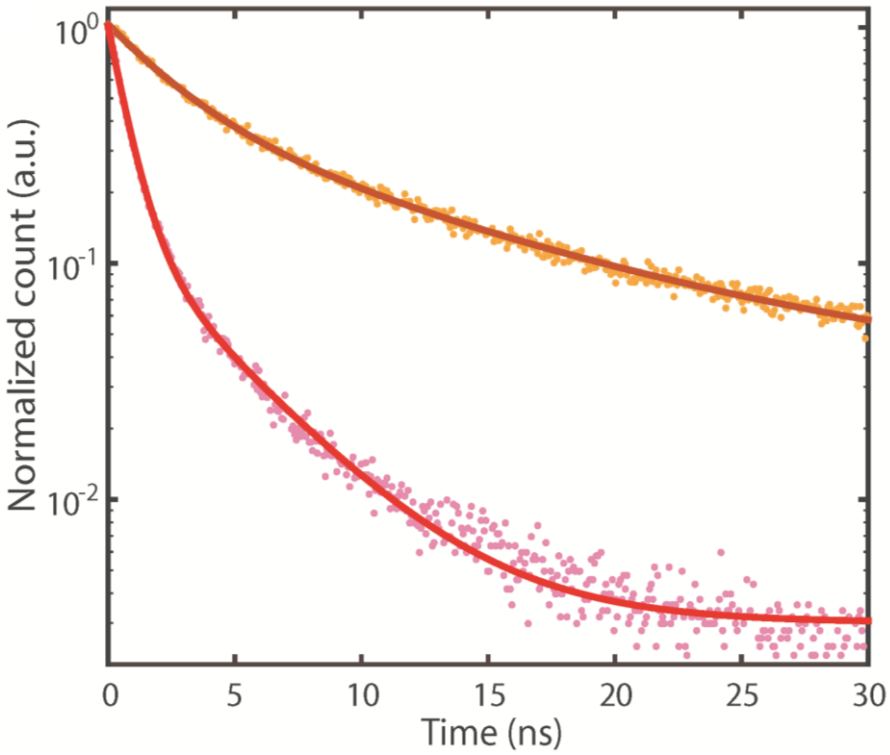

Figure 2.5 Normalized time-resolved photoluminescence from nanoplatelets on the cavity (red) and in an un-patterned region (yellow). Dots indicate the measured data, and the lines are fits to bi-exponential decays.

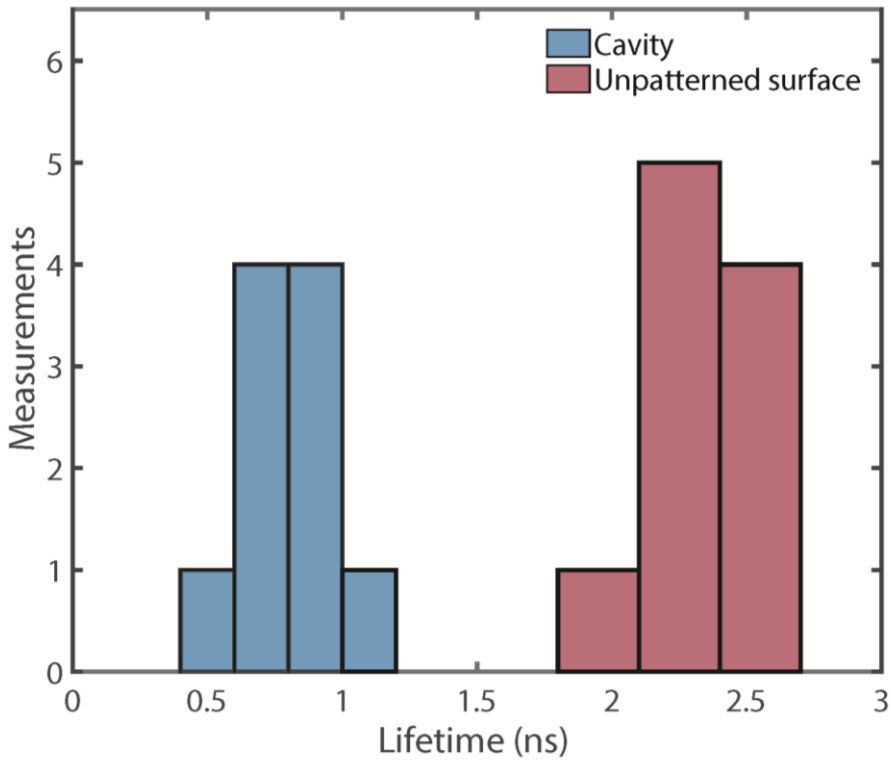

Figure 2.6 Histogram of measured lifetimes for both the un-patterned regions (purple) and the cavities (blue).

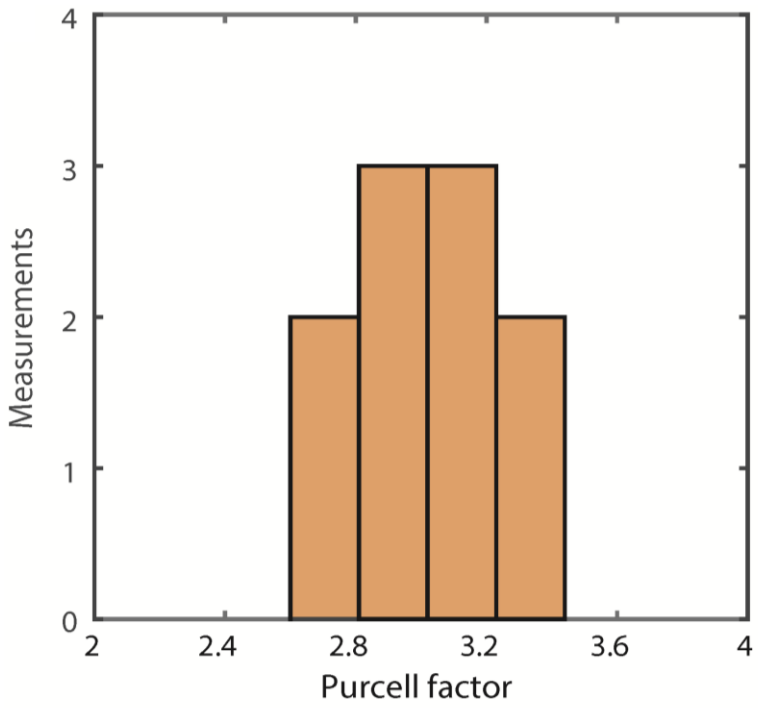

Figure 2.7 Histogram of Purcell factors determined from the lifetime measurements in

We compare the measured Purcell factor to the theoretically predicted maximum value, given by[69]

$$F_{\max} = 1 + \frac{3\lambda^3}{4\pi^2 n^2} \frac{Q_{np}}{V} \psi(r) \tag{1}$$

The above expression corresponds to the Purcell factor for an emitter located on the nanobeam surface at the location of maximum field intensity. Here, λ is the cavity-mode wavelength, $Q_{np} = \lambda / \Delta\lambda_{np}$ is the quality factor of the nanoplatelet emission line with linewidth $\Delta\lambda_{np}$, n is the refractive index of the dielectric material that makes up the cavity, $V = \int d^3\mathbf{r}\varepsilon(\mathbf{r})|E(\mathbf{r})|^2 / \left[\varepsilon(\mathbf{r})|E(\mathbf{r})|^2\right]_{\max}$ is the cavity mode volume, $\varepsilon(\mathbf{r})$ is the relative dielectric constant at the cavity frequency, and $\psi(r) = |E(r)|^2 / |E(r)|^2_{\max}$ is the ratio

of cavity-field intensity at location r to the maximum field intensity. We note that the above equation is different from the conventional expression for the spontaneous emission rate enhancement factor, which depends on the ratio of the cavity quality factor *Q* and the mode volume *V*. The conventional expression applies only in the limit where the linewidth of the emitter is much narrower than the cavity linewidth. Our system operates in the opposite regime, where the linewidth of the emitter is much broader than the cavity. In this regime, the correct expression for the Purcell factor is given by Eq. 1.[69] From finite-difference time-domain simulations, we obtain $V = 0.55(\lambda / n)^3$ and $\Psi(\mathbf{r}) = 0.36$ for an emitter located on the nanobeam surface at the field maximum. Substituting these values into Eq. 1, we obtain a maximum Purcell factor of 4.1. Thus, although the field is lower at the surface as compared to the center of the slab, the surface still provides a sufficiently large local density of states to attain a high coupling efficiency. We attribute the lower Purcell factors measured in the actual devices, as compared to the calculations, to the fact that not all of the nanoplatelets are located at the field maximum.

The measured Purcell factor provides a lower bound on the fraction of spontaneous emission coupled into the cavity mode, which we denote as β. We define the Purcell factor as $F = \frac{\tau_{\text{sub}}}{\tau_{\text{c}}} = \frac{\gamma_{\text{c}}}{\gamma_{\text{sub}}}$, where τ_{sub} is the lifetime of nanoplatelets on the un-patterned substrate, τ_{c} is the lifetime of nanoplatelets coupled to the cavity, $\gamma_{\text{c}} = \frac{1}{\tau_{\text{c}}}$ is the decay rate of a nanoplatelet in the cavity, and $\gamma_{\text{sub}} = \frac{1}{\tau_{\text{sub}}}$ is the decay rate on the un-patterned substrate. The spontaneous emission coupling efficiency is given by

$\beta = 1 - \gamma_{leak} / \gamma_c$, where $\gamma_c = \gamma_{cav} + \gamma_{leak}$; here, γ_{cav} is the nanoplatelet decay rate into the cavity mode and γ_{leak} is the decay rate of the nanoplatelets into all other radiative and non-radiative channels. An emitter inside of a cavity will typically experience Purcell enhancement when coupled to the cavity,[2] and Purcell suppression when decoupled (either due to detuning or poor spectral matching with the cavity),[3] which means that $\gamma_{leak} < \gamma_{sub}$. In this case $F < \frac{\gamma_c}{\gamma_{leak}}$ and thus $\beta > 1 - 1/F$. Using the relation $\beta > 1 - 1/F$, we obtain a lower bound of $\beta > 0.68$. This high coupling efficiency suggests that the devices should be able to support low-threshold lasing.

2.3 Characterizing lasing behavior

To investigate lasing behavior, we measure the cavity output as a function of excitation power. We plot the resulting spectra in Figure 2.8 (for a different device than the one discussed above), along with Lorentzian fits. We utilize a longer integration time for the lower pump power spectra in order to obtain enough signal to overcome the detector noise. Figure 2.9 shows the measured intensity and linewidth, determined from the Lorentzian fit, as a function of the total incident power. For the intensity, we normalize the area under the different spectra by the integration time. The intensity plot exhibits a soft threshold behavior around a pump power of 1 μW, which is characteristic of a laser with high β [70]. Using the calculated spot size of 0.38 μm in radius, this pump power corresponds to an intensity of 220 W/cm^2.

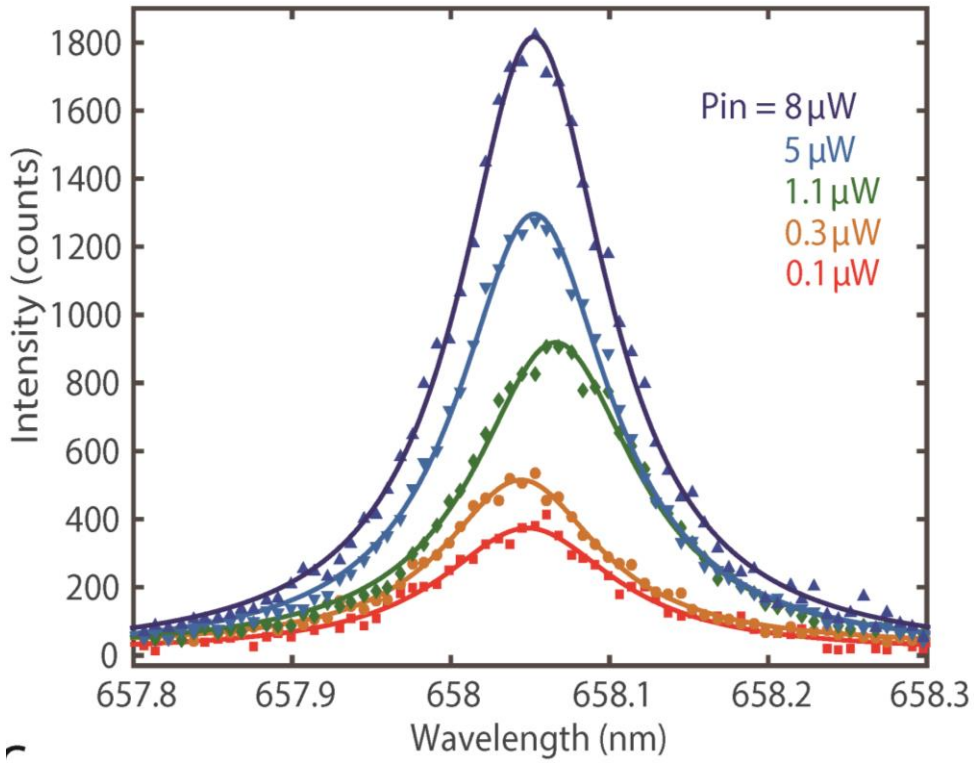

Figure 2.8 Emission spectra from nanoplatelets coupled to the cavity under different pump powers. Symbols indicate the measured data, and the lines are Lorentzian fits. Captions are pump powers for corresponding spectra in the same colors.

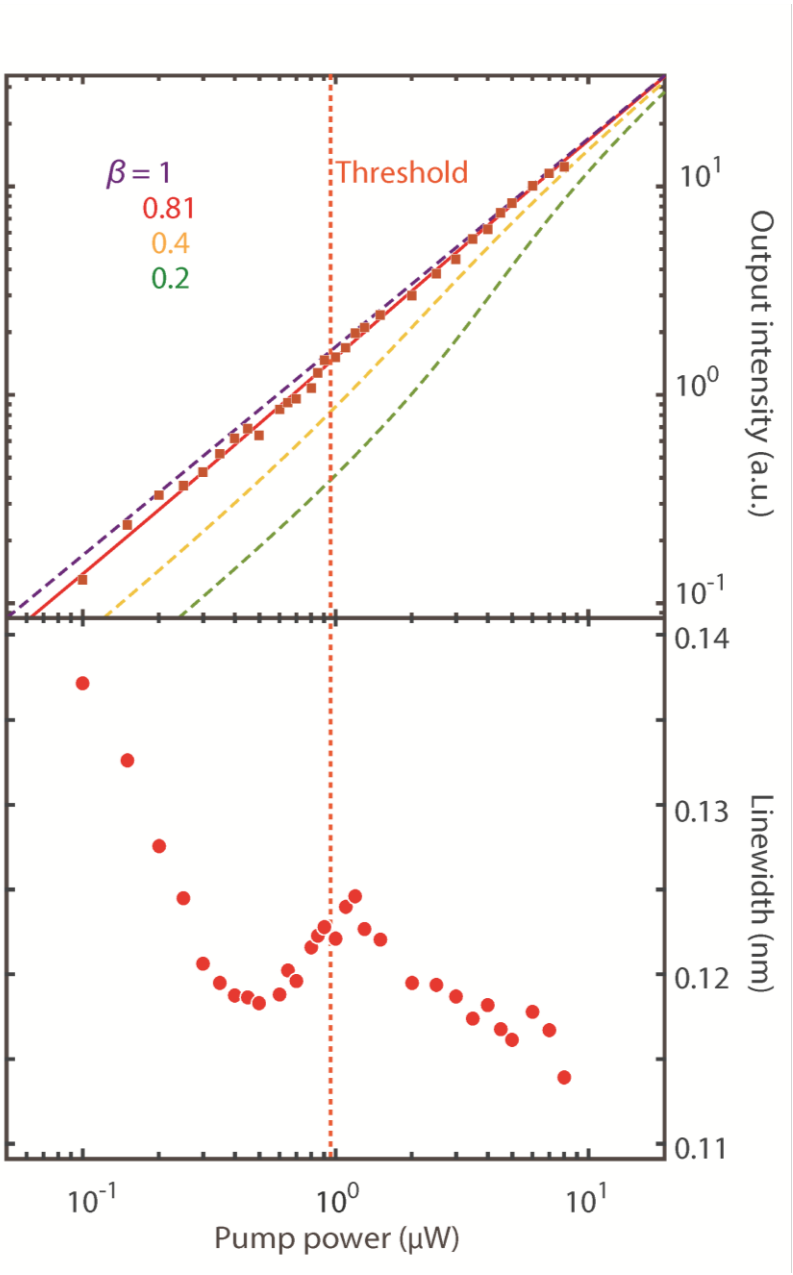

Figure 2.9 Top: Output intensity, determined from the Lorentzian fits, as a function of the total pump power. Bottom: Cavity linewidth as a function of pump power. Red squares are measured data, and the solid curve in the top panel is a fit to the laser rate equation, corresponding to a spontaneous emission coupling efficiency $\beta = 0.81$. *Dashed curves are calculation results for other values of β. The vertical dashed line (orange) indicates the lasing threshold obtained from the fit.*

2.3.1 Lasing rate equation model

To extract the spontaneous emission coupling efficiency β and the threshold P_{th} of the laser, we use a standard coupled rate-equation model for the carrier density N and the cavity photon number p of a semiconductor laser diode.

$$\frac{d}{dt}N = \frac{\eta_{\text{in}}P_{\text{in}}}{\hbar\omega_{\text{p}}V} - \frac{N}{\tau_{\text{sp}}} - \frac{N}{\tau_{\text{nr}}} - \frac{gp}{V} \tag{2}$$

$$\frac{d}{dt}p = -(\gamma - g)p + \frac{\beta V}{\tau_{\text{sp}}}N \tag{3}$$

where P_{in} is the optical power of the pump laser, η_{in} is the fraction of incident optical pump power absorbed by the gain material, $\hbar\omega_{\text{p}}$ is the photon energy of the pump laser, V is the volume of the gain medium, τ_{sp} and τ_{nr} are the exciton radiative and nonradiative lifetimes respectively, and $g = g'(N - N_0)$ is the material gain, assumed to be linearly proportional to the carrier density, where $g' = \beta V / \tau_{\text{sp}}$ is a material constant and N_0 is the transparency carrier density of the material. The cavity photon number is $p = P_{\text{out}} / \hbar\omega\gamma\eta_{\text{out}}$, where P_{out} is the output power onto the detector, ω is the cavity resonance frequency, η_{out} is the laser output collection efficiency, $\gamma = \omega / Q$ is the cavity decay rate, and β is the spontaneous emission coupling efficiency. The detected electron number on the CCD is linearly proportional to the output power ($n_{\text{ccd}} = kP_{\text{out}}$). Thus, we have $p = \alpha n_{\text{ccd}}$, where $\alpha = 1/k\hbar\omega\gamma\eta_{\text{out}}$.

The solid line in figure 2.9 is a fit to a rate-equation model (see Appendix B) which is the steady-state solution to the above rate equations[70] given by

$$P_{in} = \frac{\hbar \omega_p \gamma}{\beta \eta_{in}} \left[\frac{p}{1+p} (1+\xi)(1+\beta p) - \xi \beta p \right] \quad (4)$$

where P_{in} is the pump input power, γ is the cavity decay rate, ω_p is the pump frequency, ξ is the cavity photon number at transparency, and η_{in} is the pumping efficiency, defined as the fraction of incident pump power absorbed by the laser. We define the cavity photon number as $p = P_{out} / \hbar \omega \gamma \eta_{out}$ where P_{out} is the measured output power, ω is the cavity resonance frequency and η_{out} is the laser output collection efficiency. Figure 2.9 shows the best fit to the model in Eq. 4 as a solid line. From the fit, we determine a spontaneous coupling efficiency of $\beta = 0.81 \pm 0.03$, which is consistent with the lower bound determined from the lifetime measurements. The figure also shows, for comparison, theoretical curves for other values of β.

To show the threshold behavior more clearly, we plot the difference between the output intensity and a linear fit to the data for input powers below threshold (figure 2.10). A device with no threshold will have the same slope both above and below threshold, resulting a horizontal line. In contrast, a device with a threshold behavior will exhibit a rise in power above threshold. The measured data shows a clear nonlinear behavior with an upward inflection point at threshold. We also plot theoretical curves for several values of β.

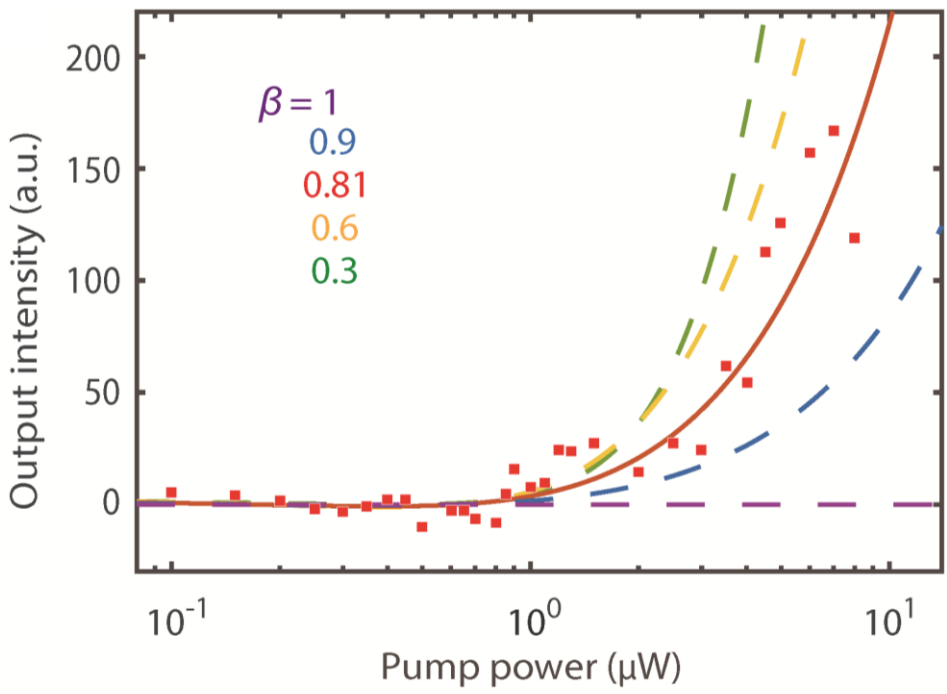

Figure 2.10 Output intensity after subtracting a linear fit to the data points below threshold. The solid curve is the fit to the laser rate equation, and dashed curves are calculated for other values of β.

The linewidth behavior (Figure 2.9 bottom) provides additional strong evidence of lasing. Below threshold, the linewidth decreases with increasing pump power due to absorption saturation and reduced spontaneous-emission noise. At threshold (indicated by the vertical dashed line), we observe linewidth broadening due to gain-index coupling, indicating the dynamic phase transition into lasing[71]. Based on the linewidth slightly below this threshold pump power, we estimate the bare cavity quality factor to be 5600. Above threshold, the linewidth again decreases due to continued suppression of spontaneous emission noise. This characteristic linewidth behavior provides a clear signature that our device reaches and exceeds the lasing threshold to attain laser oscillation.

2.3.2 Lasing threshold power

We determine the lasing threshold power from the condition where there is on average one photon in the cavity ($p=1$)[70]. Plugging this condition to Eq. 4 and inserting values from the numerical fit, we obtain a lasing threshold power of $P_{th} = P_{in}\big|_{p=1} = 0.97 \pm 0.03\ \mu\text{W}$. This threshold power accounts for all of the pump light injected into the focusing lens. Many works also report the amount of pump light absorbed by the gain material at threshold. We determine a precise value for the absorbed power using the in-coupling efficiency of η_{in}=21.6 ± 0.4% obtained from the numerical fit. This efficiency is defined as the fraction of the pump laser that is absorbed by the gain material. Multiplying this value by the threshold pump power, we calculate a threshold absorbed power of 210±10 nW, equal to the minimum power required to achieve lasing. This exceptionally low power can be attributed to the high gain provided by the nanoplatelets due to reduced Auger recombination rates compared to conventional colloidal nanocrystals[24], the high optical absorption coefficients of the nanoplatelets, and the small mode volume of the photonic-crystal cavity. Reducing the mode volume leads to an enhancement of the radiative recombination rate within the nanoplatelets; this, in turn, leads to a large fraction of spontaneous emission being coupled into the cavity. In addition, the spontaneous emission enhancement means that the nanoplatelets can support higher carrier densities before Auger recombination begins to compete with the gain.[72]

2.3.3 Lasing stability

We also examined the photostability of our device. To demonstrate the stable performance of our lasing device, we conduct a measurement on another lasing device prepared by the same method as the measured one. The pump power is kept constant at 10 μW, which is about 10 times above the threshold. From the Lorentzian fit of the acquired spectrum, we find a cavity Q of 4,900 and a resonance wavelength of 664.5 nm at the beginning of our experiment. We record the output intensity as a function of time while the device is continually excited for 3.5 hours, the result is shown in figure 2.11. For the first 2 hours of operation, the output power only decreases by 5 % over 2 hours of operation. The output power from the device drops about 20 % compared to its initial value after the entire measurement, which is likely due, at least in part, to drift in the collection efficiency for our measurement system. This stability could be further improved by incorporating better surface passivation or methods or encapsulating layers[73].

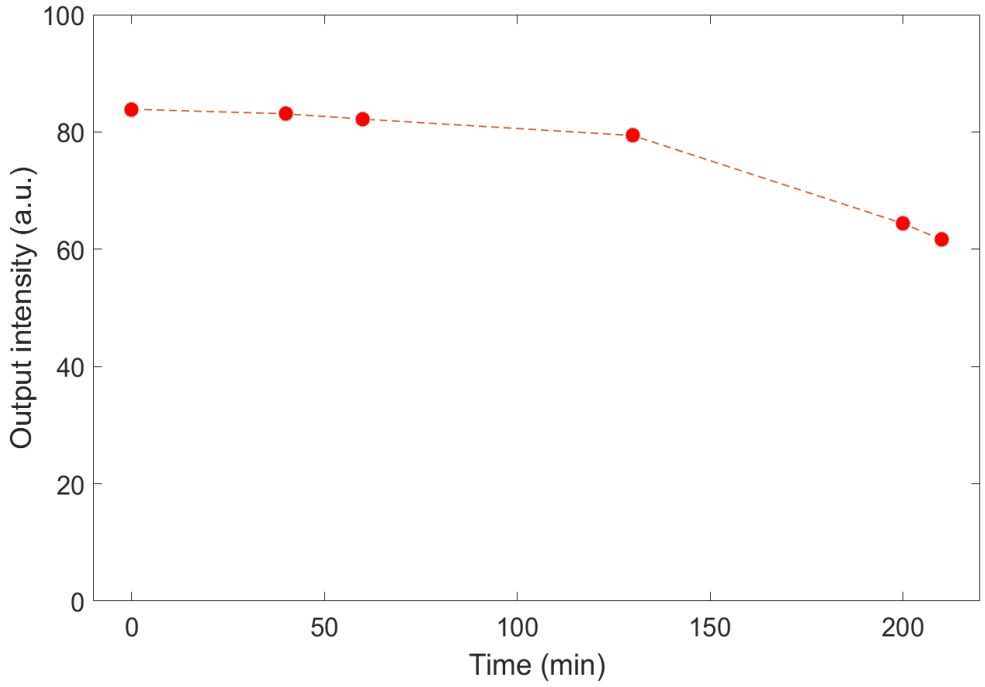

Figure 2.11 Device output intensity from Lorentzian fit of the cavity mode as a function of time.

2.4 Conclusion and discussion

In summary, we have demonstrated a nano-laser using solution-processable semiconductor nanocrystals that supports room-temperature continuous-wave operation. We attain a lasing threshold of only 0.97 μW. To put this threshold value into context, we compare it to previously reported threshold values for nano-lasers. Currently, epitaxially grown III-V semiconductor heterostructures represent some of the most advanced nano-laser material systems. A number of works reported room temperature nano-lasers with continuous-wave operation based on these materials when coupled to dielectric[29] and metallic[30] cavities. To properly compare our thresholds to these past works, we first note that multiple definitions of laser threshold

exist in the literature. The most common definition utilizes a linear fit of the of the light-in light-out curve above threshold, and defines threshold as the intersection of this fit with the x-axis[6,8,74]. Using this definition, room-temperature thresholds as low as 0.3 μW have been reported in similar nanobeam cavities using gallium arsenide quantum dots[75]. We calculate the threshold of our device based on this definition to be 200 nW. However, this definition will significantly under-estimates the threshold when applied to a high-β laser such as the one reported in Ref. 38 (the reported β is 0.88), as well as in this current work. The more fundamental definition, originally proposed by Björk and Yamamoto[70], identifies threshold as the pump power where the average cavity photon number is unity. Several works utilize this definition of threshold[36,76,77], with reported values as low as 7 μW. The threshold power we report of 0.97 μW is based on this definition. Finally, some works report the total absorbed power in the gain medium, rather than the input power. The absorbed power only accounts for the energy absorbed in the gain medium, after normalizing out imperfect overlap of the pump laser spot with the active region of the nano-laser or partial transparency of the gain medium at the pump wavelength. Our absorbed pump power is 210 nW, similar to previously reported values using indium phosphide structures that achieved sub-microwatt threshold absorbed powers for the first time[36]. Thus, in all cases our reported thresholds are similar to and often below the best numbers reported for a room-temperature laser.

We attribute the low thresholds and continuous-wave operation attained in this work to a combination of the high radiative efficiency of heterostructure colloidal nanoplatelets at room temperature, along with the reduction in threshold achieved by

employing high-Q nanocavities. We note that the heterostructure nanoplatelets can still exhibit blinking behavior that strongly depends on their environment and pumping intensity. However, since the nanolaser is composed of many nanoplatelets, we expect this blinking behavior to average out resulting in a steady continuous wave emission. Also, these cavities attain high spontaneous emission coupling efficiencies and significantly reduce the volume of the gain medium. These factors serve to significantly reduce the gain required to achieve threshold as compared to previous work based on amplified spontaneous emission[22,23], which requires larger gain materials and couples only a small fraction of spontaneous emission into the amplified modes.

We could further reduce the laser threshold by improving the cavity *Q*, which has the potential to exceed 80,000 with better fabrication[78]. Nanoplatelets also provide broad flexibility with respect to the emission wavelength. By adjusting layer thicknesses, we can tune the emission of colloidal nanoplatelets to span the entire visible range[23]. Electrical pumping methods demonstrated in colloidal quantum dot light-emitting diodes[79] may also translate to nanoplatelets to enable electrically pumped nano-lasers. Ultimately, colloidal nanoplatelets provide a promising new approach for colloidally synthesized nanophotonic devices operating at extremely low powers.

Chapter 3: Spontaneous emission enhancement of colloidal perovskites

3.1 Introduction

Solution-processable lead trihalide perovskite semiconductors are also an alternative in optoelectronic applications to epitaxial materials that are complicated to synthesize[4,38,41,42]. They exhibit a small Stokes shift[43], high charge carrier mobility[44], and large absorption coefficient[45], These features could lead to implementation of high-performance photovoltaic devices, light-emitting diodes, and light sources for efficient lasers. Previous studies focusing on photovoltaics have adopted perovskite thin films as an absorbing layer in solar cells with record-high certified conversion efficiencies of 22.1%[80]. Moreover, the material could serve as a new category of efficient emitters and gain materials in various light sources[47].

In particular, colloidal perovskite nanocrystals are promising candidates for light-emitting materials among others, such as colloidal quantum dots[81], nanorods[20], and nanoplatelets[24,82]. Perovskite nanocrystals exhibit slow nonradiative decay pathways, which leads to a lower chance of Auger recombination than other quantum emitters suffered from in the past[83]. Their exciton energy is widely tunable by chemical composition and quantum confinement[37]. This allows the emission to span the entire visible spectrum, especially purple-blue wavelengths where other colloidal quantum emitters are hard to synthesize and emit poorly. In addition, lead trihalide perovskites exhibit low defect densities, which lead to high photoluminescence efficiency at room temperature[84-86]. With these features, researchers have demonstrated light-emitting

diodes[87,88], amplified spontaneous emission[89], and lasing in large mode volume cavities[90] under high excitation. Moreover, it is preferable to further increase the efficiency and reduce lasing threshold of these devices. In order to do so, spontaneous emission rate enhancement by coupling to photonic crystal cavities could be a viable method. However, such coupling remains unexplored for cavities with mode-volume comparable to the wavelength. Also, by coupling to photonic crystal cavities, one could investigate strong light-matter interaction and cavity quantum electrodynamic applications using perovskite nanocrystals with large binding energies and oscillator strengths[91].

In this work, we demonstrate enhanced radiative emission of perovskite nanocrystals by coupling them to a silicon nitride, photonic crystal nanocavity. The cavity enhances the spontaneous emission rate of the nanocrystals by an average factor of 2.9. The Purcell effect realized here is at green wavelengths, which has been hard to achieve previously using other materials. Our results provide a path toward compact on-chip light sources with reduced energy consumption and size.

3.2 Device design and fabrication

3.2.1 $CsPbBr_3$ perovskite nanocrystals

Our device uses $CsPbBr_3$ perovskite nanocrystals. We synthesize the $CsPbBr_3$ nanocrystals in a solution and then centrifuge using the washing procedure described in our recent report[37]. Figure 3.1 presents the absorption and emission spectra of the perovskite in a toluene solution used in our experiment. They exhibit photoluminescence centered at 510 nm with a full-width at half-maximum linewidth of

20 nm. And the corresponding absorption onset is at 501 nm. Figure 3.2 displays a transmission electron microscope image of the ensemble nanocrystals after depositing the solution on the sample surface using the drop-casting method. The size of a single crystal is in the order of 10 nm in square side and the formed film on sample surface is uniform across a large area.

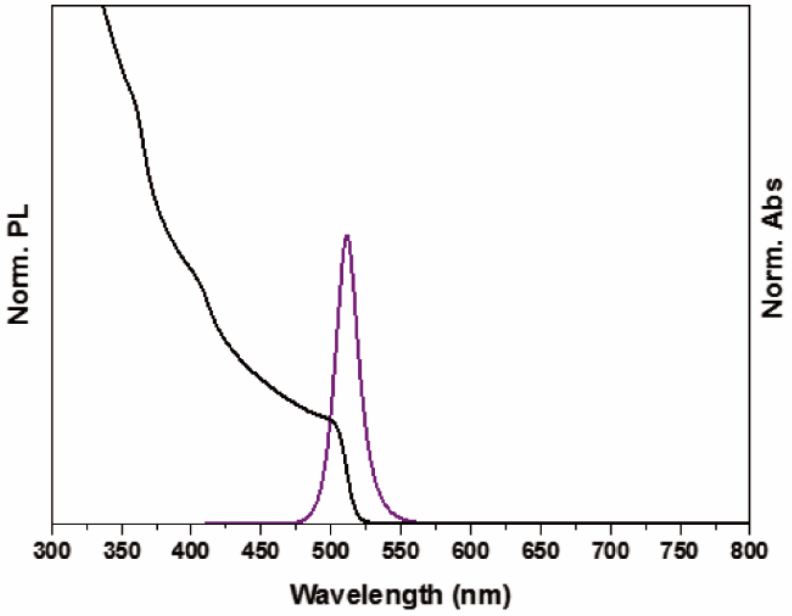

Figure 3.1 Absorption (black) and photoluminescence (purple) spectra of perovskite nanocrystals in solution form.

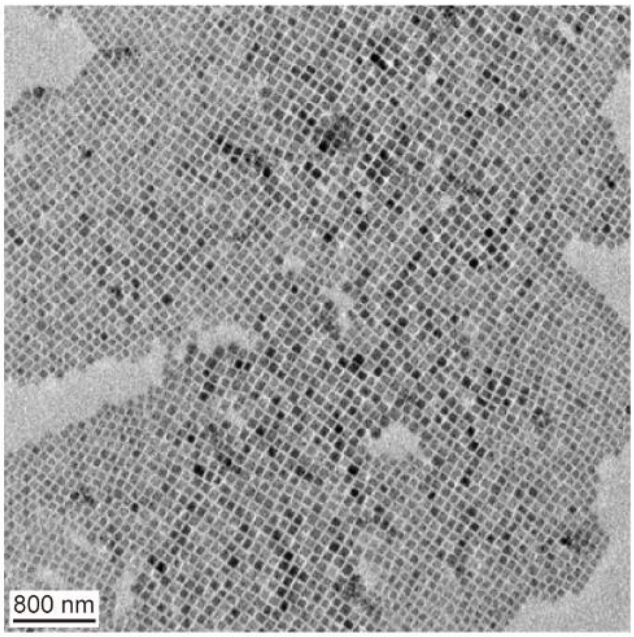

Figure 3.2 TEM image of perovskite nanocrystals deposited on a sample surface.

3.2.2 Cavity design and deposition

Similar to nanoplatelets, we again couple the perovskite nanocrystals to a silicon nitride photonic crystal nanobeam cavity designed with a cavity resonance at 510 nm[63], which is matched to the peak photoluminescence emission the perovskites. Our cavity design consists of a 200-nm-thick and 270-nm-wide SiN beam with a one-dimensional periodic array of air holes (a = 180 nm and r = 60 nm). The cavity consists of four holes at the center of the beam on both sides with linearly reduced lattice constant from 180 to 153 nm and hole radius from 60 to 45 nm. Figure 3.3 displays one fabricated device in the same way as for the nanoplatelet laser. It shows a resonant wavelength around 510 nm as designed in FDTD solutions. After fabrication, we deposit perovskite

nanocrystals onto the cavities by drop-casting a toluene solution (0.1 mg/mL) onto the sample surface.

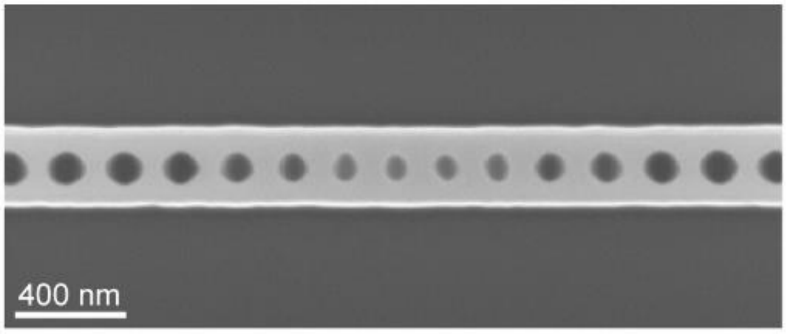

Figure 3.3 SEM image of a SiN photonic crystal nanobeam cavity.

3.3 Photoluminescence and lifetime measurements

3.3.1 Spectral enhancement

We perform the experiment under similar setup as in the previous section. Here, we only use the 70 ps duration pulsed laser at 405 nm as excitation. Figure 3.4 shows the emission spectrum of one device, as well as that from an unpatterned region of the sample (multiplied by a factor of 10) under the same excitation power of 1 μW. The photoluminescence spectrum of the perovskites at the unpatterned region has a full-width at half-maximum linewidth of 20 nm. In contrast, those coupled to the cavity mode exhibit a sharp peak emission at the cavity resonant frequency, where the signal is more than 10 times brighter than that of the unpatterned region. We note that despite the fact that we pump a smaller number of nanocrystals, we observe a much larger signal.

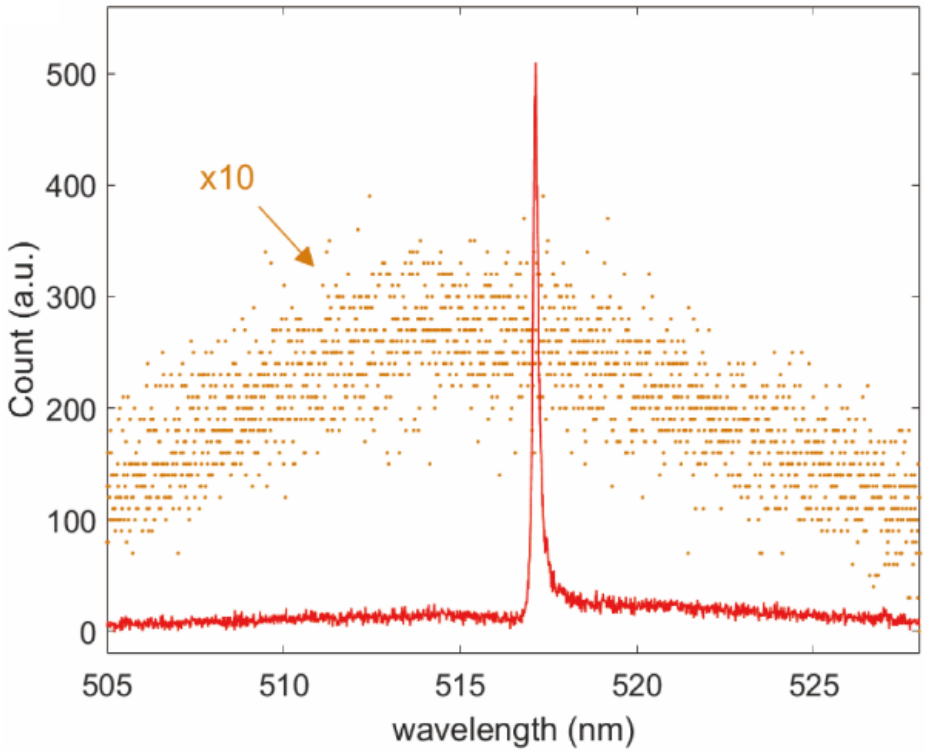

Figure 3.4 Emission spectra from perovskites on the cavity (red) and in unpatterned region (yellow, multiplied by a factor of 10 for clarity), both measured under pulsed excitation.

3.3.2 Purcell enhancement of radiative decay

We next measure radiative lifetimes of the emissions at the cavity and on the unpatterned surface. Figure 3.5 shows the time-resolved lifetime measurements for both of these cases. In both cases, the decay is multi-exponential[92], which results from the fluctuations in nonradiative pathways due to the changes in the electronic or structural environment of the material and the fact that not all excited ensemble perovskites are located at the field maximum on the cavity surface and thus are not

enhanced equally. Here, we use a stretched exponential fit to obtain the average lifetime of the ensembles:

$$I(t) = I_0 + Ae^{-(t/\tau_{se})^B} \quad (5)$$

where *I(t)* is the photoluminescence intensity at time *t*, I_0 is the background intensity, *A* is a scaling constant, $1/\tau_{se}$ is the decay rate, and *B* is the stretch parameter, which ranges from 0 to 1, indicating the variance of the decay rate (B = 1 leads to a single-exponential fit). From this stretched exponential model, we calculate the ensemble average lifetime using:

$$T_{avg} = \frac{T_{se}}{B}\Gamma(\frac{1}{B}) \quad (6)$$

where Γ is the Gamma function.

We performed lifetime measurements on 10 different devices. For each device, we also measured the unpatterned surface nearby as a comparison. The average lifetime of the perovskites on the unpatterned surface is 1.36 ± 0.60 ns with $B = 0.74$. In contrast, the cavity-coupled perovskites exhibit a shorter average lifetime of 0.46 ± 0.05 ns with $B = 0.82$. We define the Purcell factor the ratio of the cavity lifetime to the lifetime of the unpatterned surface near the cavity. From the 10 measurements, we attain an average Purcell factor of 2.9, confirming the enhancement of spontaneous emission from perovskites.

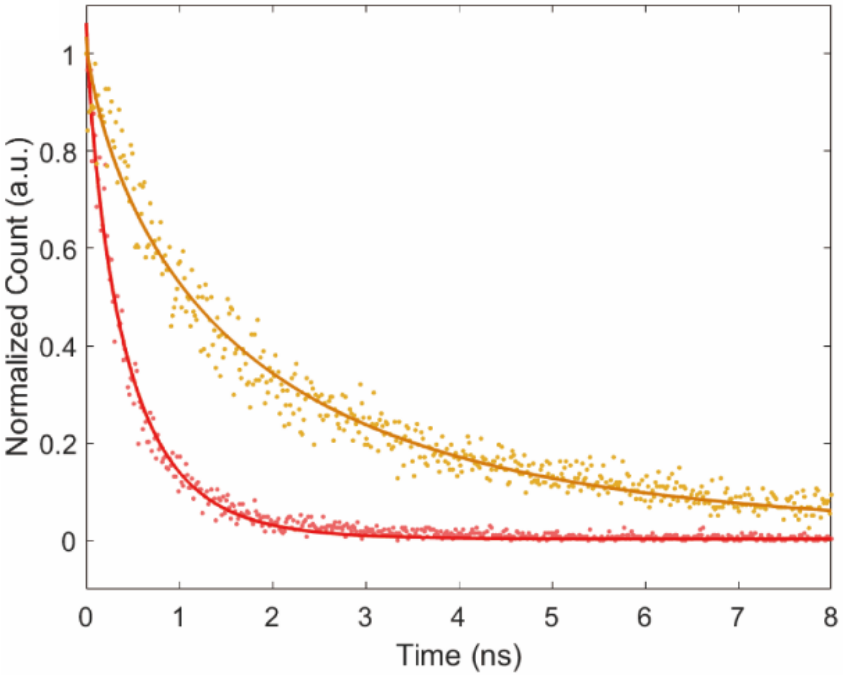

Figure 3.5 Normalized time-resolved photoluminescence from perovskites on the cavity (red) and in an unpatterned region (yellow). The dots indicate the measured data and the lines are the fits to the stretched exponential decay model.

We compare the measured lifetime to the theoretical calculation by the FDTD simulation using the same model as in the previous section (in the bad emitter regime)[69]. From simulations, we obtain $V = 0.55(\lambda / n)^3$ and $\psi(r) = 0.36$ for an emitter located at the center of the nanobeam cavity surface. Substituting these values into the model, we obtain a maximum Purcell factor of 3.6, which agrees well with the measured value. We attribute the lower Purcell factors measured in the actual devices to the fact that we are exciting an area of perovskites that are not all located at the field maximum on the nanobeam surface.

3.4 Conclusion

We have demonstrated the enhancement in intensity and radiative decay rate of the spontaneous emission from trihalide perovskite nanocrystals by coupling to a one-dimensional photonic crystal nanocavity at room temperature. We obtained a Purcell factor of 2.9 in the average spontaneous emission rate. We could further increase the enhancement by designing cavities confining the mode in the air, so that the nanocrystals will be in the region with maximum cavity-field[39]. By controlling the size and material composition we can create enhanced light emitters spanning the entire visible range, especially for the blue-green wavelengths which has been previously hard to achieve[37]. Our method could also improve the efficiency of existing perovskite LEDs to open up real world applications such as efficient illumination in display[93,94]. Finally, the results could enable lasers with low thresholds and nonlinear optical devices with fast performance, which are crucial components in integrated optoelectronics.

Chapter 4: Chiral light-matter interactions using spin-valley states in transition metal dichalcogenides

4.1 Introduction

Chiral photonic structures couple the spin of photons emitted from an emitter to the direction of propagation, which can bring new possibilities to modern optics and photonics[95,96]. The chiral light-matter interaction in the structures is useful for applications such as realization of directional spin-photon interfaces, polarization-dependent optical couplers and gates[96,97]. It also provides new platforms to investigate physical phenomena such as spin-Hall effect[98], and could ultimately paves the way towards information processing in optical networks by using the spin degree of freedom[95,96].

Researchers have studied and realized chiral light-matter interactions using atoms coupled to fibers and resonators that can exhibit polarization-dependent directional emission[99-101]. Other realization utilized quantum dots to demonstrate deterministic photon-emitter coupling[102-104]. They have also been observed in gold nanoparticles as polarization maintaining scatters coupled to nanofibers[105]. However, the emitters in these previous realizations require magnetic fields to break time-reversal symmetry of their emitting states for the chiral coupling.

For practical applications, transition metal dichalcogenide monolayers with intrinsic spin-valley states are candidates for chiral interactions without the requirement of an external magnetic field. The materials exhibit valley-dependent optical selection rules associated with orthogonal photon spins[40,106,107]. When coupled to photonic

structures, the emission can exhibit chiral light-matter interactions without the need for magnetic fields. Recent work has demonstrated chiral interfaces using WS_2 coupled to a plasmonic structures[108,109], but exhibits large ohmic losses that lead to short propagation distances. One way to significantly reduce the loss during transmission is to utilize dielectric waveguides, that we can break the mirror symmetry of the structures in design to further enhance the chiral interaction[104,110]. However, such chiral interactions between TMD monolayers and dielectric photonic structures had not been realized.

Here we experimentally demonstrate chiral light-matter interactions using spin-valley states in WSe_2 monolayers coupled to a chiral photonic crystal waveguide. We use a glide-plane photonic crystal device, which supports strong chiral light matter interactions due to broken mirror symmetry[104]. We demonstrate polarization dependent directionality of light transmission of the WSe_2 emission without an external magnetic field. This chiral interface could lead to various applications such as polarization detectors, and spin-valley dependent optical gates in integrated photonic networks[95,96]. It could also open up new approaches to utilize the spin-valley degree of freedom in TMD materials for information processing[40,111].

4.2 Composing the chiral interaction

4.2.1 Glide-plane photonic crystal waveguide

Chiral light-matter coupling exists in nanophotonic structures where the polarization of locally confined circular light locks with the mode propagation direction[96,112]. It leads to polarization or spin dependent interaction and emission

[97,103,105,113]. In order to realize chiral interactions between TMD monolayers and photonic crystal waveguides, we break the mirror symmetry in row-defect photonic crystal waveguides, that can highly enhance the chiral effect of the structures[110]. We achieve this by introducing a glide-plane dislocation, where one side of the waveguides shifts half a photonic period[104]. Therefore, the glide plane waveguides exhibit strong chiral light-matter interactions where the regions of highest chirality coincide with the regions of maximum field strength.

We adopt the glide-plane waveguide design originally proposed by Immo et. al.[104]. Parameters of the waveguide are as follows: The SiN membrane has a refractive index of n = 2.01 and a thickness of t = 200 nm, the photonic lattice constant a = 300 nm and the hole radius r = 90 nm. We choose these numbers such that the photonic crystal bandgap overlaps with the monolayer exciton and defect (bound exciton) emission. The waveguide is formed by taking out one line of holes in the middle of the photonic crystal and shifting holes on top and bottom towards the center by 50 nm. This design results in a chiral waveguide with supported modes covering the entire monolayer emission. Figure 4.1 shows simulated electric field intensity profiles in our designed glide-plane photonic waveguide induced by right and left circularly polarized dipole pairs located at local field maximum using numerical finite-difference time-domain simulations. We next project these field profiles on to right and left circularly polarized bases as shown in figure 4.2. The results here demonstrate high contrast of circular mode spatial separation and pronounced chiral effect.

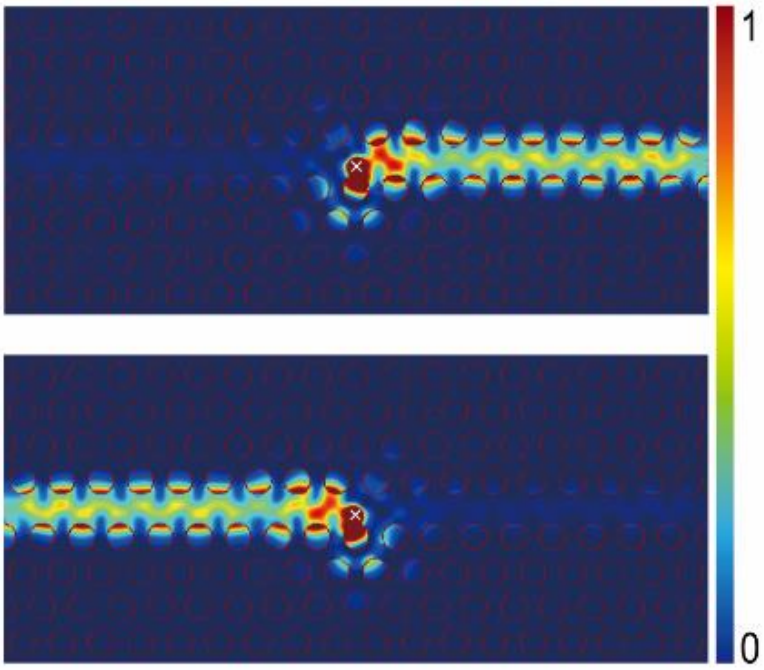

Figure 4.1 Simulated electric field intensity profiles in the glide-plane photonic waveguide induced by right (top) and left (bottom) circularly polarized dipole pairs, position of which is marked by the white cross.

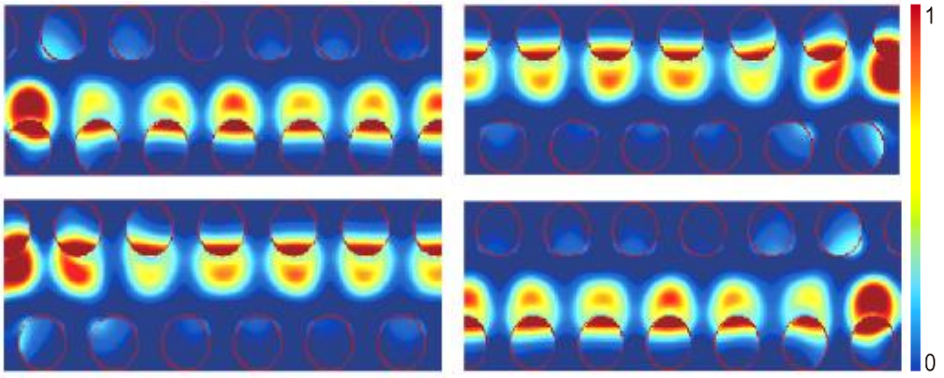

Figure 4.2 Projection of right- and left- propagating modes onto right (top) and left (bottom)circular polarization bases.

We also design grating couplers on both ends of the waveguide using a grating with 450 nm period and gradually-smaller curvature such that they can couple the monolayer emission out vertically. The fabrication process of the sample is the same as described in previous sections. Figure 4.3 shows an SEM image of one chiral waveguide structure with grating couplers at both ends.

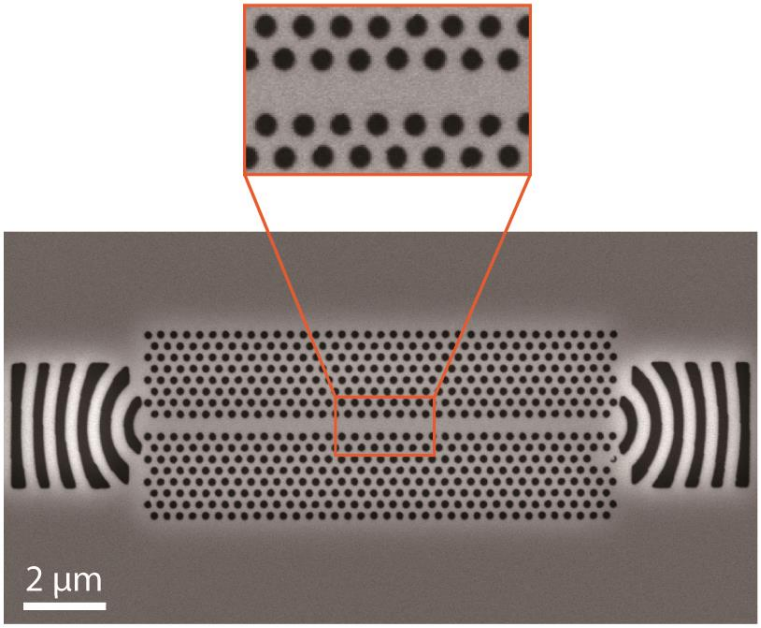

Figure 4.3 Scanning electron micrograph of the fabricated chiral photonic circuits with grating couplers at both ends.

4.2.2 Valley-spin states in WSe_2 monolayer

Transition metal dichalcogenide monolayers exhibit valley-dependent circularly-polarized optical selection rules[107]. At the two valley points (namely K and -K) in momentum space of these monolayers, strong spin-orbit coupling causing by *d* orbitals

splits the valance bands into two with spin-up and spin-down hole states as illustrated in Figure 4.4[114]. Due to time-reversal symmetry, the two valence band states of equal energy from the two valleys possess opposite hole spins, leading to opposite circular polarization selection rules. The circular polarization of input light lock with the two valleys respectively and determine the chirality of the photoluminescence emission. The circularly polarized emission with the same sign as inputs can thus chiral couple with the glide-plane waveguide mode at the chiral regions.

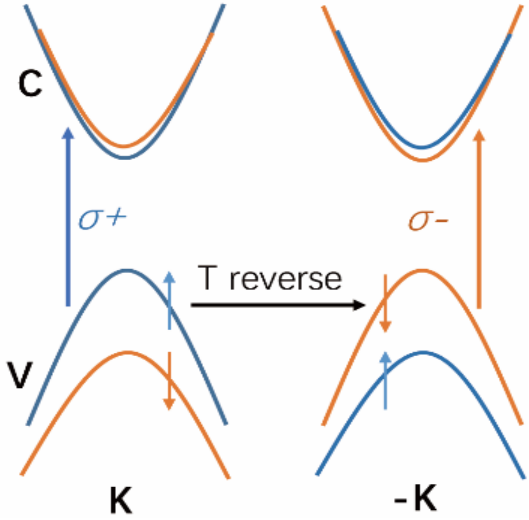

Figure 4.4 Schematic of band diagram for WSe_2 monolayers at K and -K valley points. C and V indicate conduction and valence band.

We first synthesized WSe_2 monolayers on a sapphire substrate using a chemical vapor deposition (CVD) method (see Appendix C). Figure 1.5 shows our typical CVD grown WSe_2 monolayers by our system. They are in triangular-shaped islands with size of about ten microns. We can confirm the monolayer thickness using atomic force microscope (AFM) or room temperature photoluminescence measurement since WSe_2

monolayers emit at 750 nm as shown in figure 4.5, while bilayers emit at 770 nm with much lower intensity. We assess the intrinsic valley-spin coupling effect of the WSe_2 monolayers by exciting the material with right circularly polarized light at 633 nm and collecting orthogonal circular emission respectively. The result is shown in figure 4.6 and agrees with previous reported values[114].

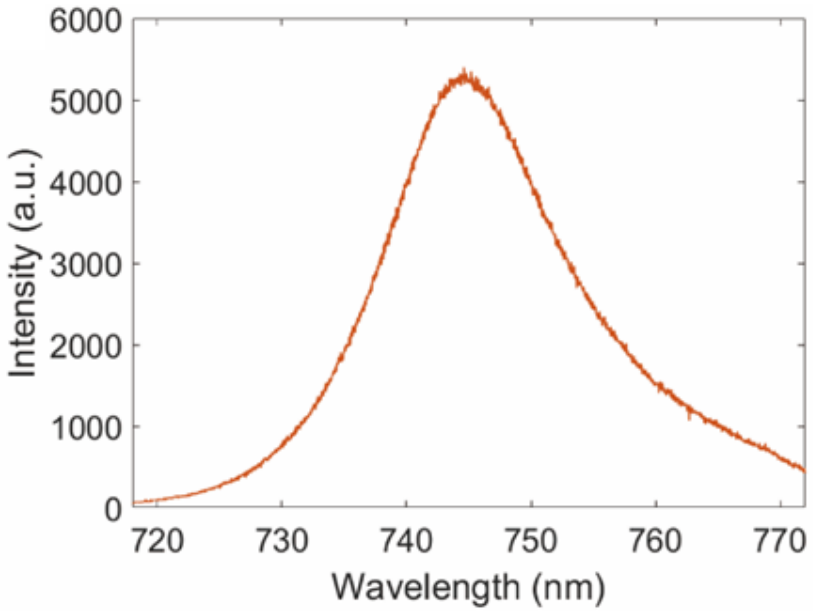

Figure 4.5 Photoluminescence emission of WSe_2 monolayers under excitation at 633 nm at room temperature.

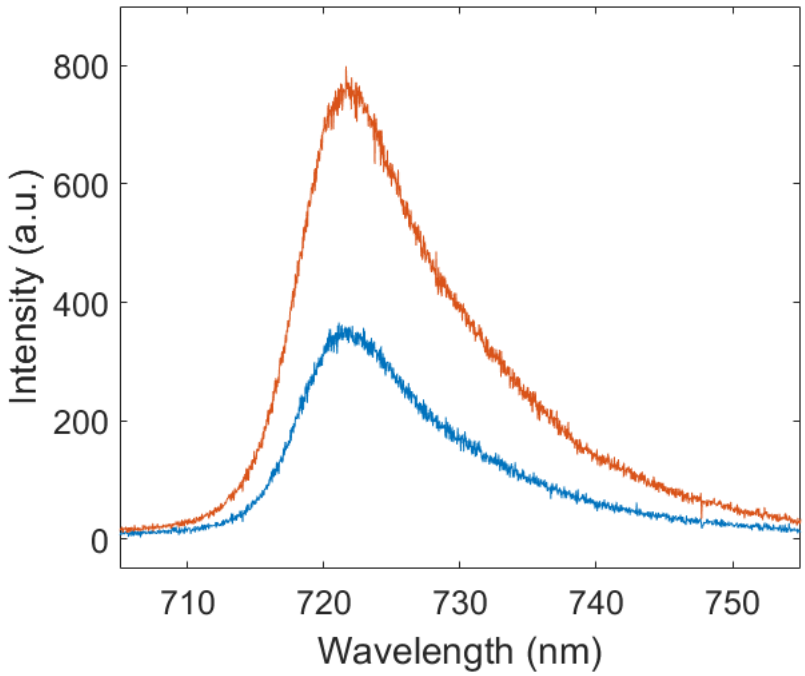

Figure 4.6 Chirality-resolved photoluminescence of WSe_2 monolayers under right circular excitation at 633 nm. Orange (blue) curves indicate right (left) circular polarization.

4.2.3 Chiral interacting system

To prepare the chiral coupled system, we first fabricate the glide-plane waveguide structures on silicon nitride on silicon wafers using electron-beam lithography and etching technics. We next precisely transfer the CVD grown WSe_2 monolayers onto the center part of our waveguide structures using a PDMS gel as transfer stamp (see Appendix C). Figure 4.7 demonstrates the schematic of the coupled system. The excitons addressed by circularly polarized input in one valley will dominantly emit light with the same helicity and preferably couple to the corresponding photonic mode propagating in one direction.

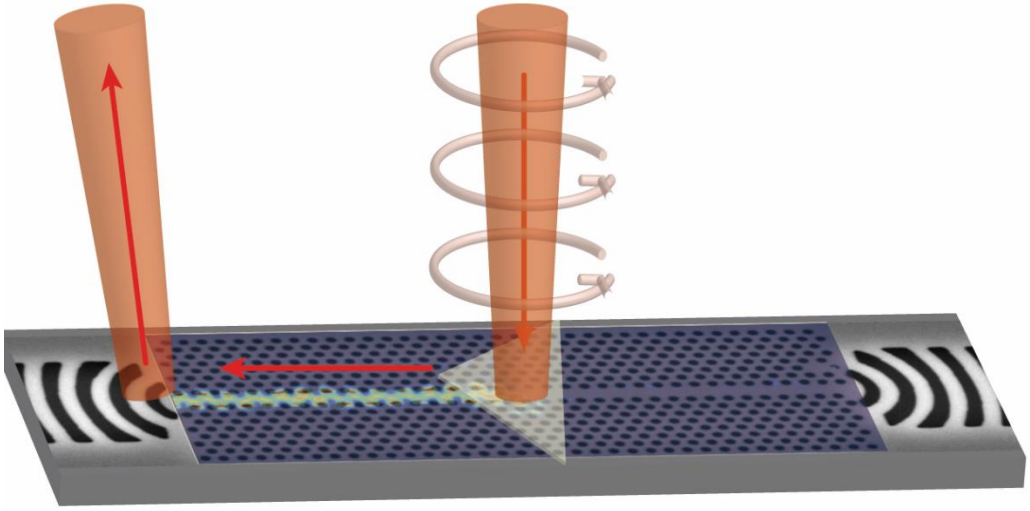

Figure 4.7 Schematic of the chiral interacting system with a monolayer flake coupled to chiral waveguide. Circularly polarized excitation will induce directional emission form one of the grating ends.

4.3 Chirality measurement

4.3.1 Nonuniform photoluminescence

We put the device into a closed-cycle cryostation which cools down to 5K and measure the performance by using the confocal microscope setup. It enables observation of samples by a camera and data collection by a spectrometer. For initial characterization, figure 4.8 and 4.9 show the optical image and the corresponding photoluminescence map under 633 nm laser excitation of the same coupled system. We consistently observe such localization and nonuniformity of photoluminescence from monolayers. One reason is that CVD-grown monolayers (typically with size of about

10 μm) break into isolated flakes with 1-2 μm sizes due to bending and pressing forces applied during our dry transfer as in figure 4.8. In addition, the nonuniformity already exists in photoluminescence from our as-grown WSe_2 monolayer flakes and also discovered in other groups[115-117]. Thus, these localized areas of bright emission could preferably couple to photonic mode propagating in one or the other direction depending on the spatial overlap of modes and the helicity of excitation.

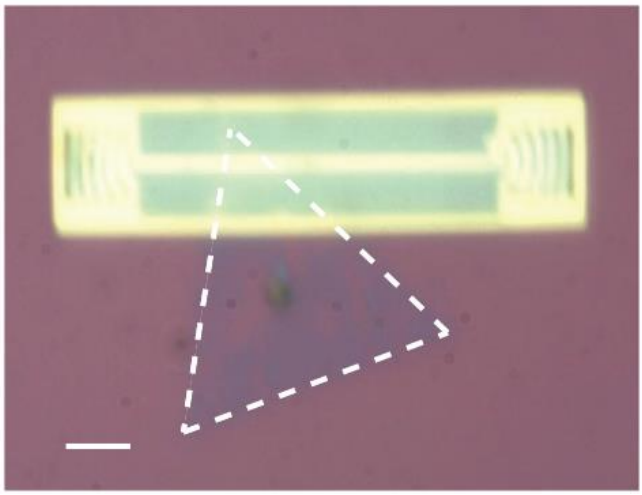

Figure 4.8 Optical image of a chiral coupled device. Dotted triangle indicates the area of a large WSe_2 monolayer flake before transfer. (bar is 2 μm)

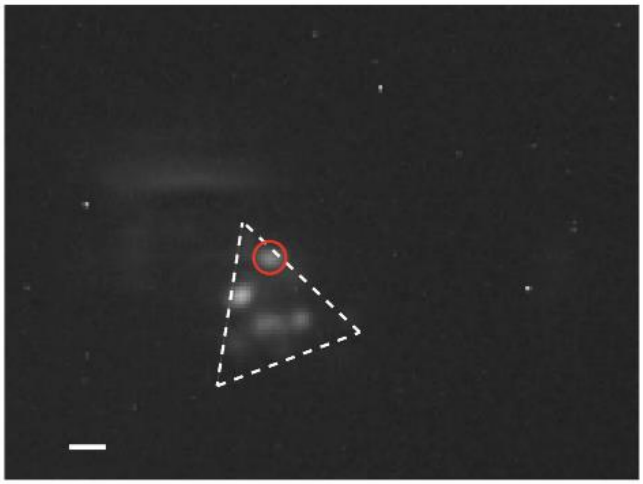

Figure 4.9 Photoluminescence map of the same chiral coupled device. The red circle indicates the coupled monolayer flake and the excitation position for the following chirality measurement.

4.3.2 Chiral coupled emission

We excite the coupled monolayer flake with orthogonal circularly polarized laser beams. The pump is on resonance with an WSe_2 exciton line at 710 nm. We detect the output signal from one and then the opposite grating ends respectively. Figure 4.10 shows the input helicity resolved spectra collected from both ends of the device. It demonstrates a pronounced chiral coupling effect of the device spanning the WSe_2 emission wavelength range. Here right circularly polarized input light predominantly addresses excitons in the K valley and generates higher signal collected from the right end compared to situation under left circular polarization. The result is reversed when collecting from the left end, with higher signal under left circular polarization. We note the periodicity in spectra is due to standing modes forming between the two waveguide ends.

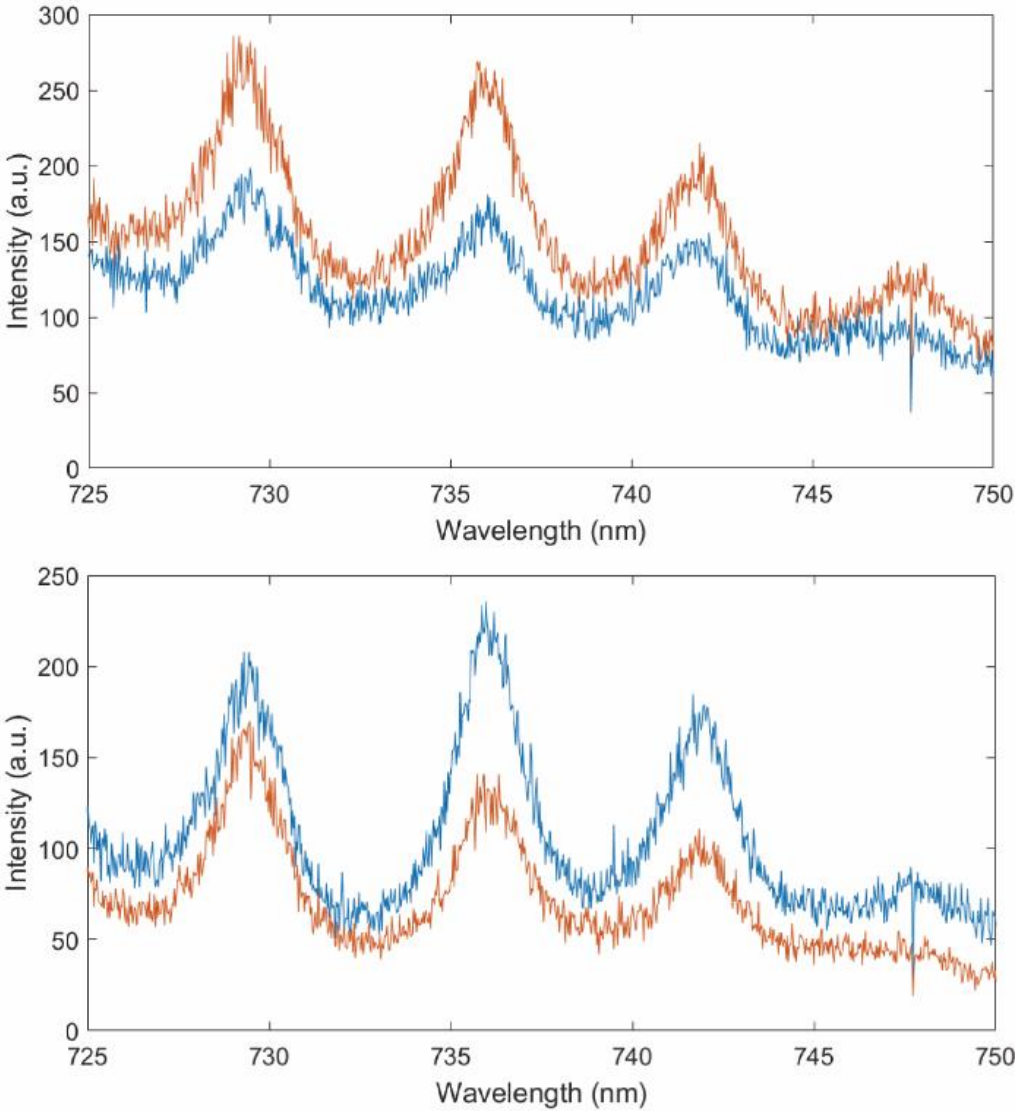

Figure 4.10 Input helicity resolved spectra collected from right (top) and left (bottom) ends. Orange (blue) curves indicate emission under right (left) circular polarization excitation.

4.3.3 Frequency-resolved directionality

To assess the chiral interaction quantitatively, we calculate the frequency-resolved emission directionality of the device for both ends using acquired spectra (figure 4.10). We define the directionality as $F_{dir}(\lambda) = (I_R(\lambda) - I_L(\lambda))/(I_R(\lambda) + I_L(\lambda))$ [], where $I_R(\lambda)$ ($I_L(\lambda)$) is the output intensity under right (left) circular polarization input at wavelength λ. To obtain the spectral-resolved directionality with minimized influence from noise, we plot the running average of $F_{dir}(\lambda)$ with a 0.5 nm bin size in figure 4.11. We observe consistent positive (negative) directionality over the WSe_2 emission range at right (left) end of the device. The result here confirms the polarization-dependent directionality and the chiral-light matter interactions of the system. Our measured directionality agrees with the upper bond limit set by the intrinsic chiral degree of polarization in WSe_2 monolayers (between 0.4 - 0.5) from our measurement and the literatures[114].

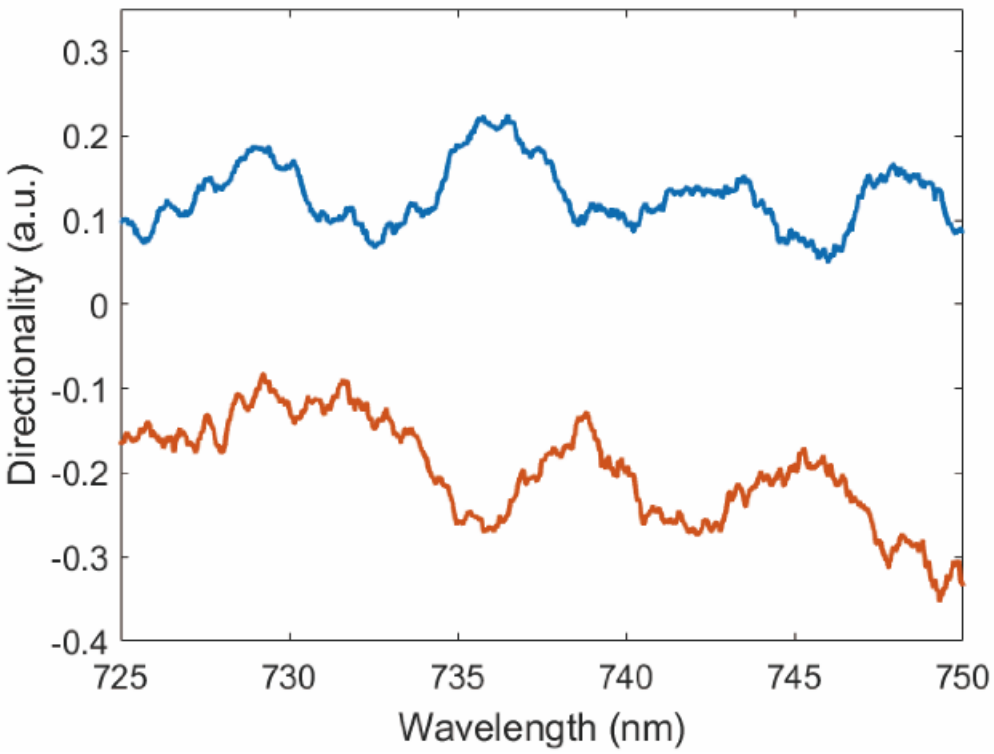

Figure 4.11 Running average of frequency resolved directionality.

4.3.4 Directionality distribution

By measuring 21 similar coupled devices, we find some devices (6 out of 21) show identical behaviour as the above one, where directionality of signals collected from right end is positive and that from the left end is negative. While some other devices (5 out of 21) possess reversed directionality, that is negative at right end and positive at left end. We define $F_{\mathrm{dir.max}}$ as the frequency resolved directionality with maximum absolute value. Its absolute value $|F_{\mathrm{dir.max}}|$ ranges from 0.15 to 0.35 for all these devices. The rest 10 devices are without pronounced chiral effect, with measurement result of one typical device shown in figure 4.12 and 4.13. They exhibit similar directionality $|F_{\mathrm{dir}}| \leq 0.1$ for all wavelengths.

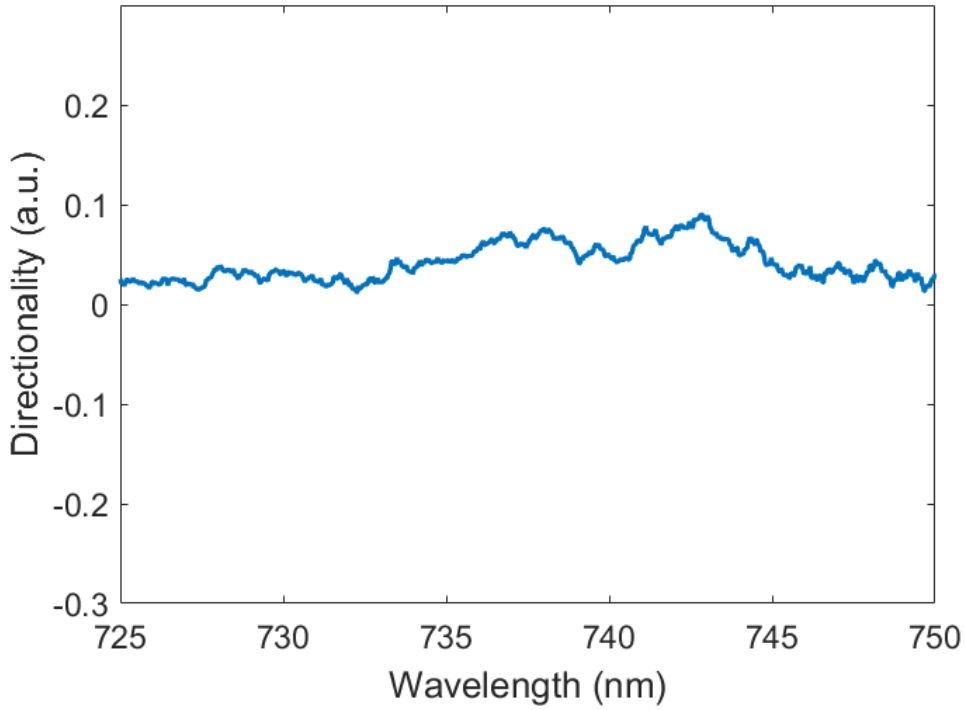

Figure 4.12 Running average of frequency resolved directionality at right port of the device without pronounced chirality.

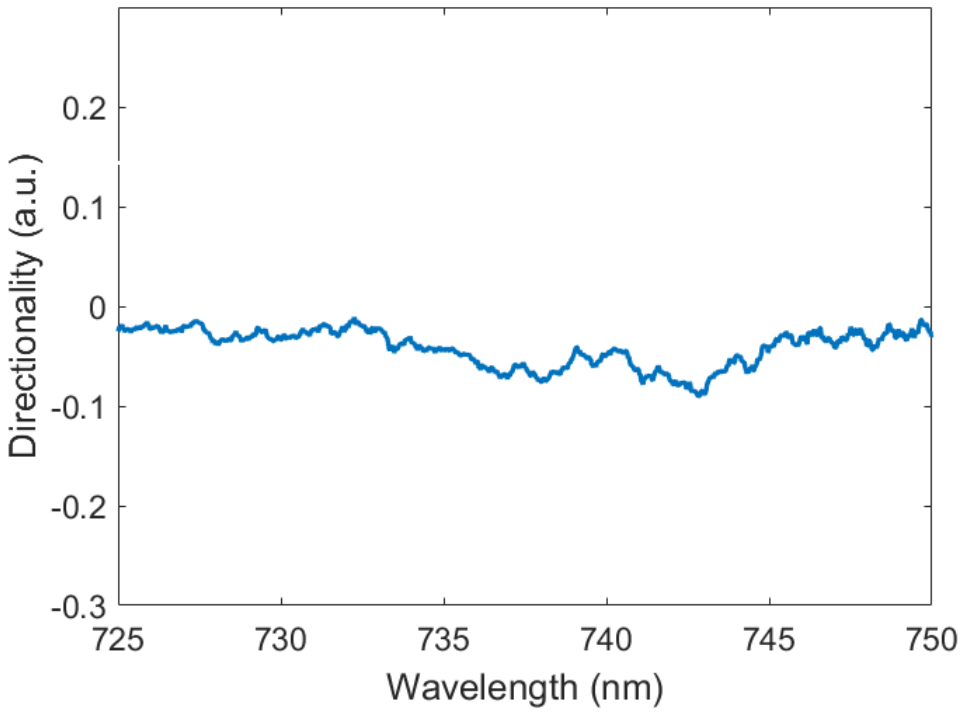

Figure 4.13 Running average of frequency resolved directionality at left port of the device without pronounced chirality.

We plot the distribution of $F_{\mathrm{dir.max}}$ at the right end of all measured devices in figure 4.14. The difference in behaviour comes from the variance of the spatial overlap between the coupled monolayer flakes and the local field maxima of photonic modes. Devices, where circularly polarized emission from monolayer flakes couples to both photonic modes almost equally, should exhibit almost no chiral effect. While the system could show pronounced chirality if the flakes spatially overlap more with the local field maxima of one helicity. This will result in a favored coupling mode and the interaction will become directional since the emission with one polarization preferably couples to one or the opposite going photonic mode. Therefore, the directionality could

also be in either way, leading to the two opposite kinds of behaviour among all chiral interacting devices.

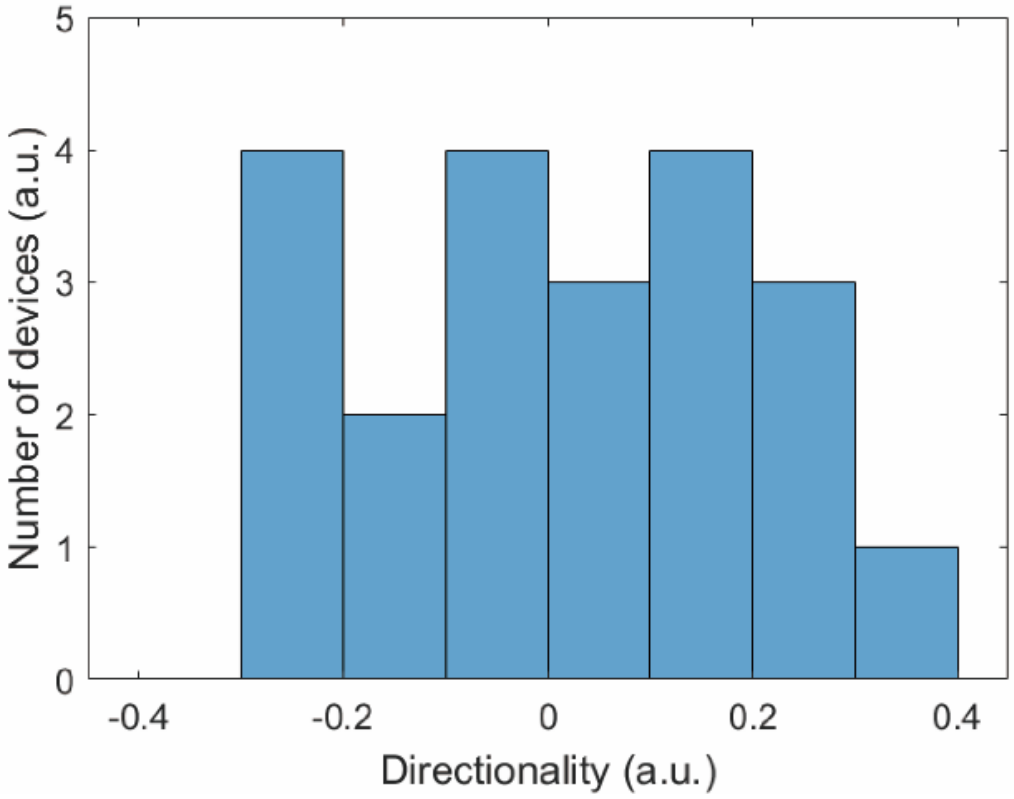

Figure 4.14 Histogram of the directionality with maximum absolute value at right end for 21 measured devices.

4.4 Conclusion

Here we demonstrate chiral light-matter interactions by coupling WSe_2 monolayers to a chiral photonic crystal waveguide structure. The system enhances on-chip control of light flow by enabling directional engineering of emission and could serve as a building block in scalable photonic platforms for optical networks and

integrated quantum information processing[95,96,118]. It also paves the way towards future exploration on the new valley-spin coupled degree of freedom in 2D semiconductors[106,111].

Chapter 5: Summary and outlook

I have demonstrated, in this thesis, different nanophotonic devices based on various low dimensional quantum emitters couple to photonic structures. They include first, demonstrating a room temperature CW nano-laser using colloidal quantum wells (nanoplatelets) coupled to a photonic crystal cavity with record-low lasing threshold below 1 μW. Furthermore, I have presented cavity-induced spontaneous emission enhancement of another colloidal emitter: perovskite nanocrystals. The final main part of the thesis is the realization of chiral light-matter interactions and the demonstration of directional light control using spin-valley states in TMDs by coupling to a glide-plane photonic waveguide.

We have utilized systems with nanobeam cavities coupled to colloidal quantum emitters, which modify and enhance their emission spectrally and temporally in intensity and efficiency. The results lead to highly efficient light sources and nano lasers that are crucial in integrated optical systems. For the last part, I showed the unique spin-valley coupling property of TMD monolayers that could introduce the new valley degree of freedom in light control and transmission. It would bring potential applications such as transmission and processing of the valley spin information in this new group of semiconductors and also lead to new ways of on-chip directional control of light.

The coupling in previous work is in the weak coupling regime where the interaction rate g between excitons and cavity photons is smaller than their average decay rates. If the interaction between exciton dipoles and the cavity photons is instead stronger than the average decay rates of the cavity photons and dipoles, the system will

be in the strong coupling regime, resulting in two new eigenstates which are half-light, half-matter cavity polariton states[119]. When entering the strong coupling regime, one could encounter a lot of interesting phenomena such as Bose-Einstein condensation, polariton superfluidity, and polariton lasing. With large exciton binding energies and sharp exciton resonances, TMD monolayers are good candidates as platforms of strong coupling in room temperature. Previous research has observed strongly coupled exciton-polaritons using MoS_2 monolayers or TMD heterostructures embedded in dielectric microcavities[120,121]. However, such effect has not been realized in WSe_2 and they are not based on nanoscale cavities with on-chip integration capability. Thus, we would like to propose different routes in order to realize strong coupling between WSe_2 monolayers and nanoscale photonic crystal cavities. The first idea is to introduce L3 or nanobeam cavities with small mode volume.

Furthermore, it would be interesting to combine the strong coupling effect with the spin-valley locking property of TMD monolayers to demonstrate strongly coupled chiral exciton-polaritons, which could lead to non-reciprocal or non-linear devices. The first option is using the chiral waveguide structure from Chapter IV since there will be standing chiral modes in between the terminated waveguide which could potentially couple the monolayer excitons. In the future we would like to investigate structures with small mode volume and tuning techniques such as gas-tuning or angle-resolved spectroscopy. We hope to realize a strongly coupled chiral exciton-polariton system, which couples these two interesting physics and leads to more complex devices such as optical diodes and transistors.

Appendices

A Nanoplatelet synthesis and characterization

We grew CdSe nanoplatelet cores using a slightly modified version of the recipe by S. Ithurria, from the work reported by M. Pelton et al[122]. In a three-necked flask, we degassed 170 mg of cadmium myristate in 15 mL of 1-octadecene (ODE) at 80^{o}C for 15 min, and then cooled down the solution to room temperature. In a nitrogen glove box (GB) we weighed out 12 mg of Se powder and added it to the degassed solution outside the GB. We then degassed the resulting mixture (cadmium myristate and Se in ODE) at 90^{o}C for 30 min. After that, we heated up the mixture rapidly, at a rate of 18 – 20^{o}C per min. In the meantime, we weighed out 40 mg of freshly ground Cd acetate dehydrate and added it to the solution at the instant when the temperature reached 190^{o}C. The mixture was still heated up quickly until 220^{o}C, whereupon we lowered the heating rate to let the mixture reach 240^{o}C without overshooting. We kept the reaction mixture at 240^{o}C for 5 min, then we rapidly cooled the mixture down to 150^{o}C, allowed it to cool down slowly to 70^{o}C, injected the solution of 2 mL of oleic acid in 10 mL of anhydrous hexane from the GB, and allowed the reaction mixture to cool down to room temperature. In the GB, we collected the reaction mixture in a centrifuge tube and centrifuged it at 5,000 rpm for 10 min to isolate the NPLs from QDs and other species in the solution. We discarded the supernatant, collected the precipitate, dispersed the latter in 4 mL of anhydrous hexane, and filtered the solution through a 0.2 μm PFTE filter. The resulting CdSe platelets luminesce at a wavelength of 512 nm, corresponding to a nominal nanoplatelet thickness of 4 monolayers.

We grew CdS shells around the CdSe cores described above by using one of the variants of the colloidal atomic layer deposition titled "c-ALD Growth in Polar Phase (e.g., NPLs). Method C" in the work by S. Ithurria and D. V. Talapin[123], with some modifications. All manipulations were performed inside the GB using anhydrous hexane, ethanol, acetonitrile, toluene, and dried N-methylformamide (NMF).

Before the growth of the first layer of CdS on the surface of CdSe NPLs, we precipitated CdSe NPLs out of the stock solution with ethanol (the amount varied between 2 and 2.5 mL), centrifuged the resulting suspension at 9000 rpm for 2 min, discarded the solution and re-dispersed the precipitate in 4 mL of hexane. We performed two such washing cycles to remove excess cadmium acetate from the synthesis.

We added 1 mL of NMF, to the washed solution, introduced 50 μL of 40 – 48% aqueous ammonium sulfide to the NMF layer, and stirred the mixture for 1 min. After the complete phase transfer from hexane to NMF, we discarded the hexane layer, added 4 mL of pure hexane, stirred the mixture, and discarded the hexane layer again. Our next step was to remove excess S^{2-} from the NMF solution of thus formed S-capped NPLs, in order to prevent secondary nucleation of CdS in the next step. To the solution, we added 1.5 mL of acetonitrile and 1 mL of toluene to precipitate the NPLs. We centrifuged the solution at 3800 rpm for 3 min, discarded the solution, and dispersed the precipitate in 1 mL of NMF. This washing procedure was repeated a second time. After the second precipitation, we re-dispersed the solution in 0.25 mL of NMF, introduced 1.75 mL of 0.2 M cadmium acetate in NMF, and stirred the solution for 1 minute. Then, we precipitated the NPLs with 4 mL toluene, centrifuged them, and re-

dispersed the precipitate in 1 mL of NMF. To the solution, we added 4 mL hexane and 200 μL of dried 70% technical-grade oleylamine. We stirred the mixture for 1 min and centrifuged it to complete the phase separation. Secondary nucleates of CdS stayed in the NMF. We collected the upper hexane layer with oleylamine-capped CdSe@CdS NPLs – the product of one cycle of the shell growth. We repeated the process of shell growth until a 4-monolayer-thick CdS shell was grown on the CdSe cores.

We deposited the CdSe core / CdS shell nanoplatelets on our nanobeam cavity sample by drop-casting. Supplementary Figure 2 shows a scanning electron microscope image of the sample after drop-casting, which shows that the nanobeam cavity is coated with a uniform layer of nanoplatelets. We note that the image does not resolve individual nanoplatelets due to the resolution limit of the SEM, and the exact thickness of the film is unknown. However, we also corroborate the uniformity of the deposition by optically exciting different unpatterned regions of the sample and observing very similar emission intensities.

B Lasing rate equation analysis

We use a standard coupled rate-equation model for the carrier density *N* and the cavity photon number *P* of a semiconductor laser diode to extract the spontaneous emission coupling efficiency β and the threshold P_{th} of the laser. It is modified from the work by G. Björk and Y. Yamamoto[70]. We use the coupled rate equations

$$\frac{d}{dt}N = \frac{\eta_{\text{in}} P_{\text{in}}}{\hbar\omega_{\text{p}} V} - \frac{N}{\tau_{\text{sp}}} - \frac{N}{\tau_{\text{nr}}} - \frac{gp}{V} \tag{5}$$

$$\frac{d}{dt}p = -(\gamma - g)p + \frac{\beta V}{\tau_{\text{sp}}} N \tag{6}$$

where P_{in} is the optical power of the pump laser, η_{in} is the fraction of incident optical pump power absorbed by the gain material, $\hbar\omega_{\text{p}}$ is the photon energy of the pump laser, V is the volume of the gain medium, τ_{sp} and τ_{nr} are the exciton radiative and nonradiative lifetimes respectively, and $g = g'(N - N_0)$ is the material gain, assumed to be linearly proportional to the carrier density, where $g' = \beta V / \tau_{\text{sp}}$ is a material constant and N_0 is the transparency carrier density of the material. The cavity photon number is $p = P_{\text{out}} / \hbar\omega\gamma\eta_{\text{out}}$, where P_{out} is the output power onto the detector, ω is the cavity resonance frequency, η_{out} is the laser output collection efficiency, $\gamma = \omega / Q$ is the cavity decay rate, and β is the spontaneous emission coupling efficiency. The detected electron number on the CCD is linearly proportional to the output power ($n_{\text{ccd}} = kP_{\text{out}}$). Thus, we have $p = \alpha n_{\text{ccd}}$, where $\alpha = 1/k\hbar\omega\gamma\eta_{\text{out}}$.

The steady-state solution to the above rate equations is

$$P_{\text{in}} = \frac{\hbar\omega\gamma}{\beta\eta_{\text{in}}}\left[\frac{p}{1+p}\left(1+\xi\right)\left(1+\beta p\right)-\xi\beta p\right] \tag{7}$$

where $\xi \equiv \frac{N_0\beta V}{\gamma\tau_{\text{sp}}}$ is the cavity photon number at transparency. We substitute $p = \alpha n_{\text{ccd}}$ into the cavity photon number and treat β, ξ, η_{in} and α as fitting parameters. From the fit, we obtain $\beta = 0.81 \pm 0.03$, and $\eta_{\text{in}} = 21.6 \pm 0.4\%$. We obtain the lasing threshold by setting $p = 1$ in Supplementary Equation 3 which gives $P_{\text{th}} = P_{\text{in}}\big|_{p=1} = 0.97 \pm 0.03\ \mu\text{W}$.

C WSe_2 synthesis and precise transfer

We synthesized WSe_2 monolayers on a sapphire substrate using the chemical vapor deposition (CVD) method. In a one-zone furnace, we put 1.5 g Se powders and 0.3 g WO_3 powders at the up-stream and the center of the furnace tube respectively[124]. A c-cut sapphire substrate is at down-stream of the tube. We heat the tube to 925^{o}C in 30 minutes while flowing Argon gas at 200 standard cubic centimeter per minute. We keep the furnace at this temperature for 15 minutes while flowing Nitrogen gas at 20 sccm and reducing the Argon gas rate to 80 sccm. Then, we stop the heater and let the whole system cool down to room temperature naturally while flowing Argon gas at 200 sccm again. During the growth process, gases carry the heated-up selenium and tungsten atoms down-stream where they deposit on the substrate, forming crystalline monolayers.

We transfer the monolayers to a polydimethylsiloxane (PDMS) substrate as an intermediate transfer medium[125]. This is done by putting a piece of PDMS gel on WSe_2 on sapphire substrate and heating the sample at 120^{o}C for 30 mins. Next, we put the sample in KOH solutions (2 g in 40 ml deionized water) for 2 hours, so the PDMS with monolayers will peel off. After cleaning with DI water, we put the PDMS stamp with the monolayer facing down to the fabricated sample using a stage system. It includes a built-in microscope and a precise 3-axis positioner, so we could accurately overlap the monolayer area with the chiral waveguide structures on the sample by seeing through the microscope on top. After contacting, we heat the sample for 2 mins at 120^{o}C and

slowly peel off the stamp. By this whole process, the monolayers will remain on the desired position at the sample surface.

Bibliography

1 Kirchain, R. & Kimerling, L. A roadmap for nanophotonics. *Nature Photonics* **1**, 303-305 (2007).

2 O'brien, J. L., Furusawa, A. & Vučković, J. Photonic quantum technologies. *Nature Photonics* **3**, 687-695 (2009).

3 Ithurria, S. *et al.* Colloidal nanoplatelets with two-dimensional electronic structure. *Nature materials* **10**, 936-941 (2011).

4 Sutherland, B. R. & Sargent, E. H. Perovskite photonic sources. *Nature Photonics* **10**, 295-302 (2016).

5 Mak, K. F. & Shan, J. Photonics and optoelectronics of 2D semiconductor transition metal dichalcogenides. *Nature Photonics* **10**, 216-226 (2016).

6 Grivas, C. & Pollnau, M. Organic solid‐state integrated amplifiers and lasers. *Laser & Photonics Reviews* **6**, 419-462 (2012).

7 Zondervan, R., Kulzer, F., Kol'chenk, M. A. & Orrit, M. Photobleaching of rhodamine 6G in poly (vinyl alcohol) at the ensemble and single-molecule levels. *The Journal of Physical Chemistry A* **108**, 1657-1665 (2004).

8 Duan, X., Huang, Y., Agarwal, R. & Lieber, C. M. Single-nanowire electrically driven lasers. *Nature* **421**, 241-245 (2003).

9 Ma, Y., Guo, X., Wu, X., Dai, L. & Tong, L. Semiconductor nanowire lasers. *Advances in Optics and Photonics* **5**, 216-273 (2013).

10 Nurmikko, A. What future for quantum dot-based light emitters? *Nature nanotechnology* **10**, 1001-1004 (2015).

11 Peng, X., Schlamp, M. C., Kadavanich, A. V. & Alivisatos, A. Epitaxial growth of highly luminescent CdSe/CdS core/shell nanocrystals with photostability and electronic accessibility. *Journal of the American Chemical Society* **119**, 7019-7029 (1997).

12 Klimov, V. I., Mikhailovsky, A. A., McBranch, D., Leatherdale, C. A. & Bawendi, M. G. Quantization of multiparticle Auger rates in semiconductor quantum dots. *Science* **287**, 1011-1013 (2000).

13 Malko, A. *et al.* From amplified spontaneous emission to microring lasing using nanocrystal quantum dot solids. *Applied physics letters* **81**, 1303-1305 (2002).

14 Cha, J. N. *et al.* Microcavity lasing from block peptide hierarchically assembled quantum dot spherical resonators. *Nano Letters* **3**, 907-911 (2003).

15 Snee, P. T., Chan, Y., Nocera, D. G. & Bawendi, M. G. Whispering‐Gallery‐Mode Lasing from a Semiconductor Nanocrystal/Microsphere Resonator Composite. *Advanced Materials* **17**, 1131-1136 (2005).

16 Dang, C. *et al.* Red, green and blue lasing enabled by single-exciton gain in colloidal quantum dot films. *Nature nanotechnology* **7**, 335-339 (2012).

17 Adachi, M. M. *et al.* Microsecond-sustained lasing from colloidal quantum dot solids. *Nature communications* **6**, 8694 (2015).

18 Guzelturk, B. *et al.* Stable and Low‐Threshold Optical Gain in CdSe/CdS Quantum Dots: An All‐Colloidal Frequency Up‐Converted Laser. *Advanced Materials* **27**, 2741-2746 (2015).

19 Hoogland, S. *et al.* A solution-processed 1.53 μm quantum dot laser with temperature-invariant emission wavelength. *Optics Express* **14**, 3273-3281 (2006).

20 Zavelani-Rossi, M., Lupo, M. G., Krahne, R., Manna, L. & Lanzani, G. Lasing in self-assembled microcavities of CdSe/CdS core/shell colloidal quantum rods. *Nanoscale* **2**, 931-935 (2010).

21 Grivas, C. *et al.* Single-mode tunable laser emission in the single-exciton regime from colloidal nanocrystals. *Nature communications* **4** (2013).

22 She, C. *et al.* Low-threshold stimulated emission using colloidal quantum wells. *Nano Lett* **14**, 2772-2777 (2014).

23 She, C. *et al.* Red, Yellow, Green, and Blue Amplified Spontaneous Emission and Lasing Using Colloidal CdSe Nanoplatelets. *ACS nano* **9**, 9475-9485 (2015).

24 Guzelturk, B., Kelestemur, Y., Olutas, M., Delikanli, S. & Demir, H. V. Amplified spontaneous emission and lasing in colloidal nanoplatelets. *ACS nano* **8**, 6599-6605 (2014).

25 Grim, J. Q. *et al.* Continuous-wave biexciton lasing at room temperature using solution-processed quantum wells. *Nature nanotechnology* **9**, 891-895 (2014).

26 Yakunin, S. *et al.* Low-threshold amplified spontaneous emission and lasing from colloidal nanocrystals of caesium lead halide perovskites. *Nature communications* **6**, 8056 (2015).

27 Pan, J. *et al.* Air-Stable Surface-Passivated Perovskite Quantum Dots for Ultra-Robust, Single-and Two-Photon-Induced Amplified Spontaneous Emission. *The journal of physical chemistry letters* **6**, 5027-5033 (2015).

28 Pelton, M. Modified spontaneous emission in nanophotonic structures. *Nature Photonics* **9**, 427-435 (2015).

29 Liang, D. & Bowers, J. E. Recent progress in lasers on silicon. *Nature Photonics* **4**, 511-517 (2010).

30 Ma, R. M., Oulton, R. F., Sorger, V. J. & Zhang, X. Plasmon lasers: coherent light source at molecular scales. *Laser & Photonics Reviews* **7**, 1-21 (2013).

31 Bose, R., Yang, X., Chatterjee, R., Gao, J. & Wong, C. W. Weak coupling interactions of colloidal lead sulphide nanocrystals with silicon photonic crystal nanocavities near 1.55 μ m at room temperature. *Applied physics letters* **90**, 111117 (2007).

32 Martiradonna, L. *et al.* Two-dimensional photonic crystal resist membrane nanocavity embedding colloidal dot-in-a-rod nanocrystals. *Nano letters* **8**, 260-264 (2008).

33 Noda, S., Fujita, M. & Asano, T. Spontaneous-emission control by photonic crystals and nanocavities. *Nature photonics* **1**, 449-458 (2007).

34 Meitner, L. Über die entstehung der β-strahl-spektren radioaktiver substanzen. *Zeitschrift für Physik A Hadrons and Nuclei* **9**, 131-144 (1922).

35 Gupta, S. & Waks, E. Spontaneous emission enhancement and saturable absorption of colloidal quantum dots coupled to photonic crystal cavity. *Optics express* **21**, 29612-29619 (2013).

36 Jang, H. *et al.* Sub-microWatt threshold nanoisland lasers. *Nature communications* **6**, 8276 (2015).

37 Protesescu, L. *et al.* Nanocrystals of cesium lead halide perovskites (CsPbX3, X= Cl, Br, and I): novel optoelectronic materials showing bright emission with wide color gamut. *Nano letters* **15**, 3692-3696 (2015).

38 Green, M. A., Ho-Baillie, A. & Snaith, H. J. The emergence of perovskite solar cells. *Nature Photonics* **8**, 506-514 (2014).

39 Quan, Q. & Loncar, M. Deterministic design of wavelength scale, ultra-high Q photonic crystal nanobeam cavities. *Optics express* **19**, 18529-18542 (2011).

40 Xu, X., Yao, W., Xiao, D. & Heinz, T. F. Spin and pseudospins in layered transition metal dichalcogenides. *Nature Physics* **10**, 343-350 (2014).

41 Kim, H.-S., Im, S. H. & Park, N.-G. Organolead halide perovskite: new horizons in solar cell research. *The Journal of Physical Chemistry C* **118**, 5615-5625 (2014).

42 Stranks, S. D. & Snaith, H. J. Metal-halide perovskites for photovoltaic and light-emitting devices. *Nature nanotechnology* **10**, 391-402 (2015).

43 Stranks, S. D. *et al.* Electron-hole diffusion lengths exceeding 1 micrometer in an organometal trihalide perovskite absorber. *Science* **342**, 341-344 (2013).

44 Leijtens, T. *et al.* Electronic properties of meso-superstructured and planar organometal halide perovskite films: charge trapping, photodoping, and carrier mobility. *ACS nano* **8**, 7147-7155 (2014).

45 De Wolf, S. *et al.* Organometallic halide perovskites: sharp optical absorption edge and its relation to photovoltaic performance. *The Journal of Physical Chemistry Letters* **5**, 1035-1039 (2014).

46 https://www.nrel.gov/pv/

47 Wang, Y. *et al.* All‐Inorganic Colloidal Perovskite Quantum Dots: A New Class of Lasing Materials with Favorable Characteristics. *Advanced materials* **27**, 7101-7108 (2015).

48 Mak, K. F., Lee, C., Hone, J., Shan, J. & Heinz, T. F. Atomically thin MoS 2: a new direct-gap semiconductor. *Physical review letters* **105**, 136805 (2010).

49 Splendiani, A. *et al.* Emerging photoluminescence in monolayer MoS2. *Nano letters* **10**, 1271-1275 (2010).

50 Zhu, Y. *et al.* Graphene and graphene oxide: synthesis, properties, and applications. *Advanced materials* **22**, 3906-3924 (2010).

51 Xia, F., Wang, H., Xiao, D., Dubey, M. & Ramasubramaniam, A. Two-dimensional material nanophotonics. *Nature Photonics* **8**, 899-907 (2014).

52 Ramasubramaniam, A. Large excitonic effects in monolayers of molybdenum and tungsten dichalcogenides. *Physical Review B* **86**, 115409 (2012).

53 He, K. *et al.* Tightly bound excitons in monolayer WSe 2. *Physical review letters* **113**, 026803 (2014).

54 Sanvitto, D. *et al.* Observation of charge transport by negatively charged excitons. *Science* **294**, 837-839 (2001).

55 Salehzadeh, O., Djavid, M., Tran, N. H., Shih, I. & Mi, Z. Optically pumped two-dimensional MoS2 lasers operating at room-temperature. *Nano letters* **15**, 5302-5306 (2015).

56 Srivastava, A. *et al.* Optically active quantum dots in monolayer WSe2. *Nature nanotechnology* **10**, 491-496 (2015).

57 Koperski, M. *et al.* Single photon emitters in exfoliated WSe2 structures. *Nature nanotechnology* **10**, 503-506 (2015).

58 He, Y.-M. *et al.* Single quantum emitters in monolayer semiconductors. *Nature nanotechnology* **10**, 497-502 (2015).

59 Kern, J. *et al.* Nanoscale Positioning of Single‐Photon Emitters in Atomically Thin WSe2. *Advanced materials* **28**, 7101-7105 (2016).

60 Kumar, S., Kaczmarczyk, A. & Gerardot, B. D. Strain-induced spatial and spectral isolation of quantum emitters in mono-and bilayer WSe2. *Nano letters* **15**, 7567-7573 (2015).

61 Englund, D. *et al.* Controlling the spontaneous emission rate of single quantum dots in a two-dimensional photonic crystal. *Physical review letters* **95**, 013904 (2005).

62 Ogawa, S., Imada, M., Yoshimoto, S., Okano, M. & Noda, S. Control of light emission by 3D photonic crystals. *Science* **305**, 227-229 (2004).

63 Khan, M., Babinec, T., McCutcheon, M. W., Deotare, P. & Lončar, M. Fabrication and characterization of high-quality-factor silicon nitride nanobeam cavities. *Optics letters* **36**, 421-423 (2011).

64 Baghani, E., O'Leary, S. K., Fedin, I., Talapin, D. V. & Pelton, M. Auger-Limited Carrier Recombination and Relaxation in CdSe Colloidal Quantum Wells. *The journal of physical chemistry letters* **6**, 1032-1036 (2015).

65 Tessier, M. *et al.* Spectroscopy of colloidal semiconductor core/shell nanoplatelets with high quantum yield. *Nano letters* **13**, 3321-3328 (2013).

66 Moss, D. J., Morandotti, R., Gaeta, A. L. & Lipson, M. New CMOS-compatible platforms based on silicon nitride and Hydex for nonlinear optics. *Nature Photonics* **7**, 597-607 (2013).

67 Kunneman, L. T. *et al.* Nature and decay pathways of photoexcited states in CdSe and CdSe/CdS nanoplatelets. *Nano letters* **14**, 7039-7045 (2014).

68 Olutas, M. *et al.* Lateral Size-Dependent Spontaneous and Stimulated Emission Properties in Colloidal CdSe Nanoplatelets. *ACS nano* **9**, 5041-5050 (2015).

69 Van Exter, M., Nienhuis, G. & Woerdman, J. Two simple expressions for the spontaneous emission factor β. *Physical Review A* **54**, 3553 (1996).

70 Björk, G. & Yamamoto, Y. Analysis of semiconductor microcavity lasers using rate equations. *Quantum Electronics, IEEE Journal of* **27**, 2386-2396 (1991).

71 Björk, G., Karlsson, A. & Yamamoto, Y. On the linewidth of microcavity lasers. *Applied Physics Letters* **60**, 304-306 (1992).

72 Gupta, S. & Waks, E. Overcoming Auger recombination in nanocrystal quantum dot laser using spontaneous emission enhancement. *Optics express* **22**, 3013-3027 (2014).

73 Chuang, C.-H. M., Brown, P. R., Bulović, V. & Bawendi, M. G. Improved performance and stability in quantum dot solar cells through band alignment engineering. *Nature materials* **13**, 796 (2014).

74 Matsuo, S. *et al.* High-speed ultracompact buried heterostructure photonic-crystal laser with 13 fJ of energy consumed per bit transmitted. *Nature Photonics* **4**, 648-654 (2010).

75 Gong, Y. *et al.* Nanobeam photonic crystal cavity quantum dot laser. *Optics express* **18**, 8781-8789 (2010).

76 Oulton, R. F. *et al.* Plasmon lasers at deep subwavelength scale. *Nature* **461**, 629-632 (2009).

77 Huang, J. *et al.* Room temperature, continuous-wave coupled-cavity InAsP/InP photonic crystal laser with enhanced far-field emission directionality. *Applied Physics Letters* **99**, 091110 (2011).

78 Quan, Q., Deotare, P. B. & Loncar, M. Photonic crystal nanobeam cavity strongly coupled to the feeding waveguide. *Applied Physics Letters* **96**, 203102 (2010).

79 Caruge, J., Halpert, J., Wood, V., Bulović, V. & Bawendi, M. Colloidal quantum-dot light-emitting diodes with metal-oxide charge transport layers. *Nature Photonics* **2**, 247-250 (2008).

80 https://www.nrel.gov/pv/

81 Shirasaki, Y., Supran, G. J., Bawendi, M. G. & Bulović, V. Emergence of colloidal quantum-dot light-emitting technologies. *Nature Photonics* **7**, 13-23 (2013).

82 She, C. *et al.* Low-threshold stimulated emission using colloidal quantum wells. *Nano letters* **14**, 2772-2777 (2014).

83 Deschler, F. *et al.* High photoluminescence efficiency and optically pumped lasing in solution-processed mixed halide perovskite semiconductors. *The journal of physical chemistry letters* **5**, 1421-1426 (2014).

84 Brandt, R. E., Stevanović, V., Ginley, D. S. & Buonassisi, T. Identifying defect-tolerant semiconductors with high minority-carrier lifetimes: beyond hybrid lead halide perovskites. *Mrs Communications* **5**, 265-275 (2015).

85 Kang, J. & Wang, L.-W. High Defect Tolerance in Lead Halide Perovskite CsPbBr3. *The Journal of Physical Chemistry Letters* **8**, 489-493 (2017).

86 ten Brinck, S. & Infante, I. Surface Termination, Morphology, and Bright Photoluminescence of Cesium Lead Halide Perovskite Nanocrystals. *ACS Energy Letters* **1**, 1266-1272 (2016).

87 Wang, J. *et al.* Interfacial Control Toward Efficient and Low‐Voltage Perovskite Light‐Emitting Diodes. *Advanced materials* **27**, 2311-2316 (2015).

88 Cho, H. *et al.* Overcoming the electroluminescence efficiency limitations of perovskite light-emitting diodes. *Science* **350**, 1222-1225 (2015).

89 Yakunin, S. *et al.* Low-threshold amplified spontaneous emission and lasing from colloidal nanocrystals of caesium lead halide perovskites. *Nature communications* **6** (2015).

90 Zhu, H. *et al.* Lead halide perovskite nanowire lasers with low lasing thresholds and high quality factors. *Nature materials* **14**, 636-642 (2015).

91 Zheng, K. *et al.* Exciton binding energy and the nature of emissive states in organometal halide perovskites. *The journal of physical chemistry letters* **6**, 2969-2975 (2015).

92 Fisher, B. R., Eisler, H.-J., Stott, N. E. & Bawendi, M. G. Emission intensity dependence and single-exponential behavior in single colloidal quantum dot fluorescence lifetimes. *The Journal of Physical Chemistry B* **108**, 143-148 (2004).

93 Xiao, Z. *et al.* Efficient perovskite light-emitting diodes featuring nanometre-sized crystallites. *Nature Photonics* **11**, 108-115 (2017).

94 Wang, N. *et al.* Perovskite light-emitting diodes based on solution-processed self-organized multiple quantum wells. *Nature Photonics* **10**, 699-704 (2016).

95 Bliokh, K. Y., Rodríguez-Fortuño, F., Nori, F. & Zayats, A. V. Spin–orbit interactions of light. *Nature Photonics* **9**, 796 (2015).

96 Lodahl, P. *et al.* Chiral quantum optics. *Nature* **541**, 473-480 (2017).

97 Young, A. B. *et al.* Polarization engineering in photonic crystal waveguides for spin-photon entanglers. *Physical review letters* **115**, 153901 (2015).

98 Bliokh, K. Y., Gorodetski, Y., Kleiner, V. & Hasman, E. Coriolis effect in optics: unified geometric phase and spin-Hall effect. *Physical review letters* **101**, 030404 (2008).

99 Junge, C., O'Shea, D., Volz, J. & Rauschenbeutel, A. Strong coupling between single atoms and nontransversal photons. *Physical review letters* **110**, 213604 (2013).

100 Shomroni, I. *et al.* All-optical routing of single photons by a one-atom switch controlled by a single photon. *Science* **345**, 903-906 (2014).

101 Mitsch, R., Sayrin, C., Albrecht, B., Schneeweiss, P. & Rauschenbeutel, A. Quantum state-controlled directional spontaneous emission of photons into a nanophotonic waveguide. *Nature communications* **5**, 5713 (2014).

102 Lodahl, P., Mahmoodian, S. & Stobbe, S. Interfacing single photons and single quantum dots with photonic nanostructures. *Reviews of Modern Physics* **87**, 347 (2015).

103 Luxmoore, I. *et al.* Interfacing spins in an InGaAs quantum dot to a semiconductor waveguide circuit using emitted photons. *Physical review letters* **110**, 037402 (2013).

104 Söllner, I. *et al.* Deterministic photon–emitter coupling in chiral photonic circuits. *Nature nanotechnology* **10**, 775-778 (2015).

105 Petersen, J., Volz, J. & Rauschenbeutel, A. Chiral nanophotonic waveguide interface based on spin-orbit interaction of light. *Science*, 1257671 (2014).

106 Xiao, D., Liu, G.-B., Feng, W., Xu, X. & Yao, W. Coupled spin and valley physics in monolayers of MoS 2 and other group-VI dichalcogenides. *Physical Review Letters* **108**, 196802 (2012).

107 Mak, K. F., He, K., Shan, J. & Heinz, T. F. Control of valley polarization in monolayer MoS2 by optical helicity. *Nature nanotechnology* **7**, 494-498 (2012).

108 Chervy, T. *et al.* Room Temperature Chiral Coupling of Valley Excitons with Spin-Momentum Locked Surface Plasmons. *ACS Photonics* **5**, 1281-1287 (2018).

109 Gong, S.-H., Alpeggiani, F., Sciacca, B., Garnett, E. C. & Kuipers, L. Nanoscale chiral valley-photon interface through optical spin-orbit coupling. *Science* **359**, 443-447 (2018).

110 Le Feber, B., Rotenberg, N. & Kuipers, L. Nanophotonic control of circular dipole emission. *Nature communications* **6**, 6695 (2015).

111 Schaibley, J. R. *et al.* Valleytronics in 2D materials. *Nature Reviews Materials* **1**, 16055 (2016).

112 Bliokh, K. Y. & Nori, F. Transverse and longitudinal angular momenta of light. *Physics Reports* **592**, 1-38 (2015).

113 Coles, R. *et al.* Waveguide-coupled photonic crystal cavity for quantum dot spin readout. *Optics express* **22**, 2376-2385 (2014).

114 Jones, A. M. *et al.* Optical generation of excitonic valley coherence in monolayer WSe2. *Nature nanotechnology* **8**, 634-638 (2013).

115 Clark, G. *et al.* Vapor-transport growth of high optical quality WSe2 monolayers. *APL Materials* **2**, 101101 (2014).

116 Liu, B. *et al.* Chemical vapor deposition growth of monolayer WSe2 with tunable device characteristics and growth mechanism study. *ACS nano* **9**, 6119-6127 (2015).

117 Zhang, X.-Q., Lin, C.-H., Tseng, Y.-W., Huang, K.-H. & Lee, Y.-H. Synthesis of lateral heterostructures of semiconducting atomic layers. *Nano letters* **15**, 410-415 (2014).

118 Žutić, I., Fabian, J. & Sarma, S. D. Spintronics: Fundamentals and applications. *Reviews of modern physics* **76**, 323 (2004).

119 Weisbuch, C., Nishioka, M., Ishikawa, A. & Arakawa, Y. Observation of the coupled exciton-photon mode splitting in a semiconductor quantum microcavity. *Physical Review Letters* **69**, 3314 (1992).

120 Liu, X. *et al.* Strong light–matter coupling in two-dimensional atomic crystals. *Nature Photonics* **9**, 30-34 (2015).

121 Dufferwiel, S. *et al.* Exciton–polaritons in van der Waals heterostructures embedded in tunable microcavities. *Nature communications* **6** (2015).

122 Pelton, M., Ithurria, S., Schaller, R. D., Dolzhnikov, D. S. & Talapin, D. V. Carrier cooling in colloidal quantum wells. *Nano letters* **12**, 6158-6163 (2012).

123 Ithurria, S. & Talapin, D. V. Colloidal atomic layer deposition (c-ALD) using self-limiting reactions at nanocrystal surface coupled to phase transfer between polar and nonpolar media. *Journal of the American Chemical Society* **134**, 18585-18590 (2012).

124 Huang, J.-K. *et al.* Large-area synthesis of highly crystalline WSe2 monolayers and device applications. *ACS nano* **8**, 923-930 (2013).

125 Castellanos-Gomez, A. *et al.* Deterministic transfer of two-dimensional materials by all-dry viscoelastic stamping. *2D Materials* **1**, 011002 (2014).